

## Episodic Mixing and Buoyancy-Sorting Representations of Shallow Convection: A Diagnostic Study

MING ZHAO AND PHILIP H. AUSTIN

*Atmospheric Science Programme, Department of Earth and Ocean Sciences, University of British Columbia,  
Vancouver, British Columbia, Canada*

(Manuscript received 9 May 2002, in final form 24 September 2002)

### ABSTRACT

Episodic mixing and buoyancy-sorting (EMBS) models have been proposed as a physically more realistic alternative to entraining plume models of cumulus convection. Applying these models to shallow nonprecipitating clouds requires assumptions about the rate at which undilute subcloud air is eroded into the environment, an algorithm to calculate the eventual detrainment level of cloud–environment mixtures, and the probability distribution of mixing fraction. A diagnostic approach is used to examine the sensitivity of an EMBS model to these three closure assumptions, given equilibrium convection with known large-scale forcings taken from phase III of the Barbados Oceanographic Meteorological Experiment (BOMEX). The undilute eroding rate (UER) is retrieved and found to decrease exponentially with height above cloud base, suggesting a strong modulation by the cloud size distribution. The EMBS model is also used to calculate convective transport by individual clouds of varying thickness. No single cloud from this ensemble can balance the large-scale BOMEX forcing; the observed equilibrium requires a population of clouds with a cloud size distribution that is maximum for small clouds and decreases monotonically with cloud size.

The EMBS model depends sensitively on the assumptions governing the detrainment of positively buoyant mixtures. In particular, given the requirement that positively buoyant mixtures detrain at their neutral buoyancy level, there is no positive definite undilute eroding rate that is consistent with the BOMEX forcing. The model is less sensitive to the assumed distribution of cloud–environment mixtures, given a multiple mixing treatment of positively buoyant parcels and detrainment at the unsaturated neutral buoyancy level.

### 1. Introduction

Shallow cumulus clouds play a fundamental role in the vertical redistribution of energy and moisture in the lower troposphere. While their influence is well established, there are currently a wide range of approaches to represent the ensemble effect of these clouds in large-scale models. This breadth of approach is understandable given the lack of consensus on the mechanism by which turbulent clouds mix with their surroundings (e.g., Blyth 1993; Emanuel 1994; Siebesma 1998). Early modeling work (e.g., Simpson 1971), represented clouds as ascending, laterally entraining plumes, with environmental air mixed homogeneously through a horizontal cloud level. Over the last 3 decades, observations and models of cumulus clouds have raised doubts about the applicability of the entraining plume concept. Observational studies from a wide range of field experiments in individual clouds suggest that the distribution of cloud properties at any given level is typically nonho-

mogeneous, and that cloudy air often has compositions consistent with two-sample mixing between undilute subcloud air (USCA) and the environmental air from near or above the observation level (e.g., Austin et al. 1985; Blyth et al. 1988; Paluch 1979). A fundamental problem with entraining plume models was pointed by Warner (1970), who observed that it was impossible for such models to simultaneously reproduce realistic values of liquid water content and cloud-top height.

Recently, a family of cloud models characterized by episodic mixing of USCA and environmental air has been designed to account for the inhomogeneity of cloud entrainment and mixing (e.g., Raymond and Blyth 1986, hereafter RB86; Emanuel 1991, hereafter E91; Hu 1997). Associated conceptual models such as the shedding thermal model have been proposed as a mechanism for such entrainment and mixing processes (e.g., Blyth et al. 1988; Blyth 1993). In this conceptual model entrainment is primarily associated with intermittent ascending thermals, which are detached from the subcloud layer as they ascend. The ascending cloud top consists of a rising USCA core with a toroidal circulation. This advancing cloud top induces forced downdrafts of environmental air that are mixed with the USCA slightly below the advancing top. The resulting mixed parcels

---

*Corresponding author address:* Ming Zhao, Department of Earth and Ocean Sciences, University of British Columbia, Vancouver, BC V6T 1Z4, Canada.  
E-mail: mzhao@eos.ubc.ca

have reduced buoyancy and are left behind in a trailing wake. Further mixing and dilution will prevent these mixtures from rising appreciable distances. The USCA in the ascending thermals is continually eroded until all the USCA has been mixed with the surrounding environment or it reaches a level where its negative buoyancy causes it to stop rising. With this mechanism the mixed air at each level consists of two sample mixtures of USCA and environmental air from slightly above the level of observation, in agreement with observations (e.g., Blyth et al. 1988). Recent high-resolution simulations of nonprecipitating cumulus clouds from Carpenter et al. (1998) lend some support to the shedding thermal concept.

The strength of the observational support for the shedding thermal model is still a matter of debate. Recently Neggers et al. (2002) have pointed out that, although undilute air has been found at all levels within cumulus clouds (e.g., Heymsfield et al. 1978; Jensen et al. 1985), it represents only a small fraction of the cloud, and therefore is unlikely to be responsible for all cloud mixing and dilution. However, a numerical simulation of nonprecipitating cumulus cloud led Carpenter et al. (1998) to conclude that undilute thermals are responsible for most of the entrainment and detrainment due to their vigorous ascent, even though they occupy only a small part of the overall area of the upper portion of modeled clouds. Recent radar observations (Kollias et al. 2001) show the presence of unmixed updrafts penetrating about 150 m into the capping inversion and extending for 400 m in the vertical and 250–300 m in the horizontal for a 700-m-thick cumulus cloud. This is consistent with a considerable amount of USCA existing at higher cloud levels, although such USCA parcels will presumably be short-lived. Aircraft measurements of these undilute cumulus cores are more difficult, particularly for shallow cumuli, due to their short lifetimes and their inherent spatial and temporal variability.

While further mixing and dilution of the USCA–environment mixtures might also be important, most episodic mixing models simplify this process by moving the initially generated mixtures to their neutral buoyancy levels (NBLs) where they are detrained to the environment. This “buoyancy sorting” is based on the idea that individual samples of cloud–environment mixture tend to move toward their NBL (e.g., Telford 1975; Taylor and Baker 1991). Although highly idealized, episodic mixing and buoyancy sorting (EMBS) models account for in-cloud inhomogeneity, resolve the cloud-top liquid water paradox, and also accommodate features such as downdrafts that can not be represented explicitly in entraining plume models. However, EMBS models require the specification of three pieces of information for which there are few observational constraints: the mixing rate at which USCA is eroded into the environment [which we will refer to as the “undilute eroding rate” (UER)], the probability distribution of the mixing fraction (called the “mixing distribution” below) following a mixing

event, and an algorithm (called the “detrainment criterion” below) to both account for subsequent mixing between the mixed parcel and its environment, and to redistribute cloud–environment mixtures through the column following the detrainment of cloud air.

In this study we adapt an EMBS model to study convection in a field of shallow nonprecipitating cumulus clouds. For the case of an equilibrium atmosphere it is possible to diagnose an UER given a mixing distribution and detrainment criterion and then examine the transport predicted by the EMBS model. We use this framework to test the sensitivity of the EMBS approach to commonly used choices for the mixing distribution and the detrainment criterion. In section 2 we introduce EMBS models in general and our adaptation in particular, and discuss the range of closure assumptions adopted in current models. We derive the diagnostic expression for the UER, given an algorithm for detraining cloud–environment mixtures and an atmosphere in equilibrium with large-scale forcings for entropy and moisture. In section 3 we diagnose the UER for a particular case, the undisturbed trade wind boundary layer from phase III of the Barbados Oceanographic and Meteorological Experiment (BOMEX), and offer an interpretation for the form of the resulting UER in terms of the individual transport contributions of clouds with a range of sizes. We conclude this section with an analysis of the sensitivity of the retrieved UER to the mixing distribution, and the impact of the detrainment criterion on the EMBS model. Section 4 provides a summary and discussion.

## 2. Approach

In this section we review the EMBS framework together with common choices for the mixing distribution and detrainment criterion. We describe an EMBS model in which the mixing and detrainment terms depend linearly on the UER for nonprecipitating cumulus clouds. Given this linear dependence it is possible to diagnose the vertical profile of the UER for an equilibrium boundary layer with known large-scale forcings.

### a. Mass flux parameterization

For an environment containing nonprecipitating cumulus clouds with small cloud fraction, the conservation equations for environmental entropy and total water, averaged over a region containing many clouds, can be written as (e.g., Arakawa and Schubert 1974; Emanuel 1994)

$$\begin{aligned} \frac{\partial \theta_i}{\partial t} + \mathbf{V}_H \cdot \nabla \theta_i - \rho g w \frac{\partial \theta_i}{\partial p} + Q_R \\ = \underbrace{-g M_f \frac{\partial \theta_i}{\partial p}}_I + \underbrace{g(\theta_{i,c} - \theta_i) D}_{II} \end{aligned} \quad (1a)$$

$$\begin{aligned} \frac{\partial q_t}{\partial t} + \mathbf{V}_H \cdot \nabla q_t - \rho g w \frac{\partial q_t}{\partial p} \\ = \underbrace{-gM_f \frac{\partial q_t}{\partial p}}_I + \underbrace{g(q_{t,c} - q_t)D}_II, \end{aligned} \quad (1b)$$

where  $\theta_l$  is liquid water potential temperature and  $q_t$  is total water specific humidity (see appendix A for a complete list of symbols).

The rhs terms of (1) are tendencies due to cumulus subgrid-scale transport. Term I represents the effect of cloud-induced environmental compensating vertical motion, with  $M_f$  denoting the average vertical cloud mass flux. This mass flux can take on either positive or negative values for typical shallow cumulus layers, either heating and drying or cooling and moistening the environment. Term II represents lateral detrainment of the entropy and moisture difference between cloudy air ( $\theta_{l,c}$ ,  $q_{t,c}$ ) and the environment; it is generally a moistening and cooling effect. Terms I and II are coupled by cumulus entrainment and mixing, one of the most important processes in nonprecipitating cumulus dynamics and thermodynamics. To close (1), we need to further parameterize  $M_f$ , the detrained cloud properties  $\theta_{l,c}$ ,  $q_{t,c}$ , and detrainment rate of cloud air mass  $D$ .

### b. EMBS model notation

In this section we introduce the procedure for calculating terms I and II of (1) on a vertically discretized grid for an EMBS model. Given vertical level  $i$  between cloud base ( $i = \text{ICB}$ ) and cloud top ( $i = \text{ICT}$ ), we denote the upward flux of USCA at interface level  $i + 1/2$  as  $F^{i+1/2}$ , and write the change of  $F$  over the depth of level  $i$  as  $U^i = F^{i-1/2} - F^{i+1/2}$ , where  $U^i$  is the eroded USCA mass flux at discretized level  $i$  and has units of  $\text{kg m}^{-2} \text{s}^{-1}$ . The UER at level  $i$ , which is defined as the vertical gradient of the undilute mass flux, is given by  $E^i = -(dF/dz)^i \approx U^i/\Delta z$ , where  $\Delta z$  is the layer thickness,  $E^i$  has units of  $\text{kg m}^{-3} \text{s}^{-1}$  and is resolution independent. Given these definitions,  $F^b$ , the undilute cloud-base mass flux, is  $F^b = \sum_{i=\text{ICB}}^{\text{ICT}} U^i$ .

At each level  $i$ ,  $N$  mixtures are generated between USCA with values of entropy and total water ( $\theta_l^u$ ,  $q_t^u$ ) and environmental air with ( $\theta_l^e$ ,  $q_t^e$ ). Assuming that mixing is strictly linear, the conserved thermodynamic variables for individual mixture  $j$  are given by

$$\theta_l^{i,j} = \sigma^j \theta_l^e + (1 - \sigma^j) \theta_l^u \quad (2a)$$

$$q_t^{i,j} = \sigma^j q_t^e + (1 - \sigma^j) q_t^u, \quad (2b)$$

where  $\sigma^j$  is the fraction of environment air in the  $j$ th mixture in the range  $0 < \sigma^j < 1$ .

Figure 1 gives an example of ( $\theta_l^{i,j}$ ,  $q_t^{i,j}$ ) mixtures for a representative trade cumulus sounding of  $\theta_l$ ,  $q_t$ , and  $\theta_v$  (BOMEX phase III, see section 3a for additional detail). The cloud-base height (600 m) and cloud-top

height (2000 m) are determined respectively by the lifting condensation level (LCL) and the neutral buoyancy level of the USCA at the top of the surface layer at 120 m (not shown). The vertical distance between levels in Fig. 1 is 40 m. The dots at each level represent  $N = 20$  mixtures generated using (2), ranging linearly from purely USCA (0% environment air) to highly dilute (95% environment) air. To provide a specific focus for discussion, four numbered boxes in Fig. 1 show the coordinates for three negatively buoyant mixtures with liquid water contents ranging from unsaturated (mixture 1) to saturated with small liquid water content ( $0.22 \text{ g kg}^{-1}$ , mixture 2) to saturated with large liquid water content ( $1.87 \text{ g kg}^{-1}$ , mixture 3). Mixture 4 at the 1000-m level is positively buoyant and saturated.

Before we discuss the  $\theta_v$  values of Fig. 1c, we consider Fig. 1d, which shows  $\theta_v^{i,j}$  and  $\theta_l^{i,j}$  for a single mixing spectrum generated at cloud top. Figure 1d shows that while the mixtures' conservative variables  $\theta_l^{i,j}$  and  $q_t^{i,j}$  ( $q_t^{i,j}$  not shown) are strictly linear during the mixing, the mixtures' buoyancy variable  $\theta_v^{i,j}$  varies nonlinearly with the mixing fraction ( $\sigma^j$ ). The panel also shows that all mixtures at the cloud-top level are negatively buoyant due to the evaporation of liquid water during the mixing process. Since the environment air is warm and dry, only a small proportion of environment air is needed for an USCA–environment mixture to achieve significant negative buoyancy (e.g., mixture 3).

The blue and green dots in Fig. 1c are negatively buoyant mixtures generated by mixing between positively buoyant USCA and the environment throughout the cloud levels. Two general features can be seen from the panel. The first is that only a very small fraction of saturated mixtures are negatively buoyant below the inversion, while a much larger fraction are negatively buoyant above the inversion. This is consistent with the finding in large eddy simulations (LESs) that few saturated downdrafts are present below the inversion, but a significant number are observed above the inversion (de Roode and Bretherton 2003). Second, about half of the cloud–environment mixtures are unsaturated and negatively buoyant, if we assume a uniform mixing distribution. The fraction of unsaturated mixtures should be increased beyond this, given that, in nonprecipitating cumuli, all saturated mixtures have to be further mixed and eventually evaporated. Since unsaturated mixtures are invisible and have thermodynamic properties close to those of their environment, they can be easily neglected in either observations or analysis of numerical simulations. Compared with the visible part of the cumulus cloud little quantification has been done on this part of cumulus convection, which may also play an important role in vertical mass transport.

The points of Fig. 1 span all possible cloud environment mixtures with  $0 < \sigma^j < 1$ . Left undetermined is the probability distribution of mixing fraction  $P(\sigma^j)$  for the mixture spectrum generated at each model level. To illustrate our use of the mixing distribution in an EMBS

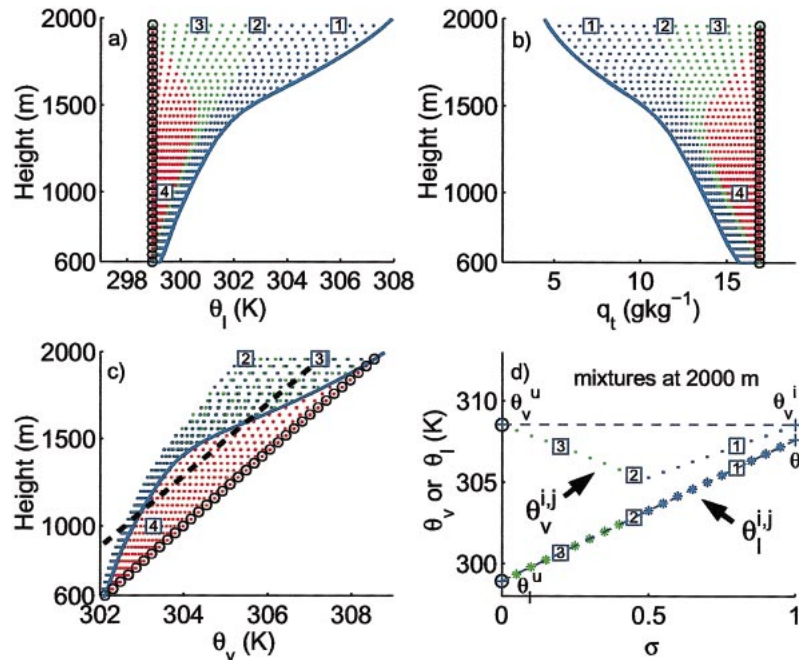


FIG. 1. (a)–(c) Vertical ( $\theta$ ,  $q_t$ ,  $\theta_v$ ) profiles of mixtures generated by the episodic mixing hypothesis. The solid lines are the BOMEX sounding. Black circles represent ascending USCA. At each level, a portion mixes with environmental air and generates a spectrum of mixtures (dots). Red dots are positively buoyant saturated mixtures, green dots are negatively buoyant saturated mixtures, and blue dots are negatively buoyant unsaturated mixtures. Numbered labels are described in the text. Dashed line in (c) is the moist adiabat. (d) The mixture spectrum generated at the cloud-top level (2000 m);  $\sigma$  is the fraction of environmental air in mixtures.

model, consider  $U^i$ , the eroded USCA mass flux at level  $i$ . The model first divides  $U^i$  into undilute subparcels according to an assumed mixing distribution. Each subparcel is labeled with index  $j$ , and will mix with environment air, with environment fraction given by  $\sigma^j$ . The resulting eroded USCA mass flux for subparcel  $j$  is therefore

$$u^{i,j} = P(\sigma^j)U^i, \quad (3)$$

where  $P(\sigma^j)$  is the normalized distribution of the eroded USCA mass flux in the spectrum of mixtures. The total mass flux of the mixture  $j$  is

$$m^{i,j} = \frac{u^{i,j}}{1 - \sigma^j}. \quad (4)$$

Given the thermodynamic properties and the individual mixture's  $m^{i,j}$ , we can calculate its detrainment level and its associated mass flux contribution to levels between the mixing level  $i$  and its detrainment level. In the next section we discuss the choice of detrainment level, while in section 2d we review four choices of  $P(\sigma^j)$ .

### c. Detrainment criterion

Given  $\theta_l^{i,j}$ ,  $q_t^{i,j}$ , and a pressure level, we can calculate all other thermodynamic properties of a mixture, as il-

lustrated in Fig. 1c for  $\theta_v$ . The liquid water virtual potential temperature  $\theta_v^{i,j}$  will also be used below. It is the  $\theta_v$  obtained by reversible adiabatic evaporation of a mixture liquid water, and is nearly conserved for adiabatic motion in shallow clouds (Emanuel 1994). In the buoyancy sorting stage of an EMBS model,  $\theta_v$  or  $\theta_{lv}$  is compared against the environment to determine the detrainment level of each mixture. RB86, for example, assume that mixed parcels exit the cloud at their NBL, where the parcel and environment have equal  $\theta_v$ . A problem with this detrainment, as pointed out by Taylor and Baker (1991), is that cloudy air detrained at its NBL will become negatively buoyant upon mixing with its subsaturated environment. E91 addresses this by detraining mixtures at their unsaturated neutral buoyancy level (UNBL), defined as the level where the parcel and environment have equal  $\theta_{lv}$ . This is equivalent to defining a cloud–environment boundary such that all evaporation of liquid water occurs within cloud. Such a cloud boundary is larger than the actual visible cloud and includes a near-cloud region that is free of liquid water but part of the cloud-induced convective circulation.

Figure 2 shows the very different consequences of these two detrainment assumptions for shallow cumulus clouds. Figures 2a–c and 2d–f show the final location of each of the mixtures in Fig. 1, given the detrainment assumptions of RB86 and E91 respectively. As required

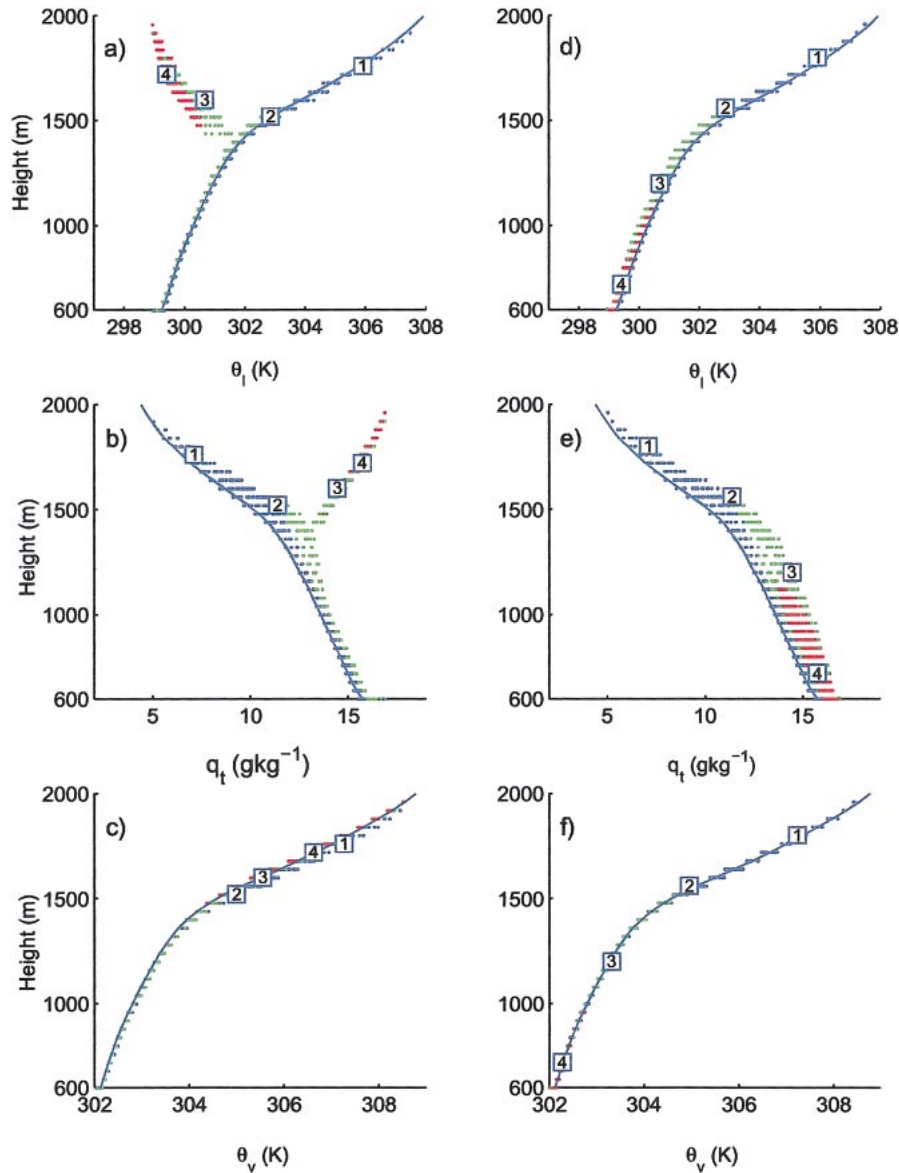


FIG. 2.  $\theta_l$ ,  $q_t$ , and  $\theta_v$  of mixtures from Fig. 1 following buoyancy sorting. (a)–(c) The NBL (RB86) detrainment assumption; (d)–(f) the UNBL (E91) detrainment. Dot colors and labels are as in Fig. 1.

by buoyancy sorting, all mixtures in Figs. 2c and 2f collapse (with small deviations due to finite vertical resolution) to the environmental  $\theta_v$ . Labeled mixtures 1–4 correspond to those of Fig. 1, transported to their new equilibrium levels. A comparison of Figs. 2c and 2f reveals that the detrainment criteria of both RB86 and E91 require unsaturated mixture 1 to descend dry adiabatically to roughly 1800 m and detrain. Similarly, mixture 2 with little liquid water descends, first moist adiabatically for a short distance (parallel to the moist adiabat shown in Fig. 1c), then follows a dry adiabat (vertically) to detrain at roughly 1500 m under both detrainment assumptions. In contrast, mixture 3, with

its larger liquid water content, is detrainment at an NBL of approximately 1600 m under the detrainment criterion of RB86, where its  $\theta_v$  matches that of the environment. Under the UNBL detrainment assumption of E91, the mixture evaporates its liquid water and descends further to  $\approx 1200$  m, where the environment and mixture  $\theta_v$  values are equal. Finally, positively buoyant mixture 4 is transported well into the inversion under the detrainment assumption of RB86, but evaporates its liquid water and descends to 700 m using the UNBL criterion of E91.

Under the NBL detrainment criterion, mixtures 3 and 4, which are comparatively undilute following initial

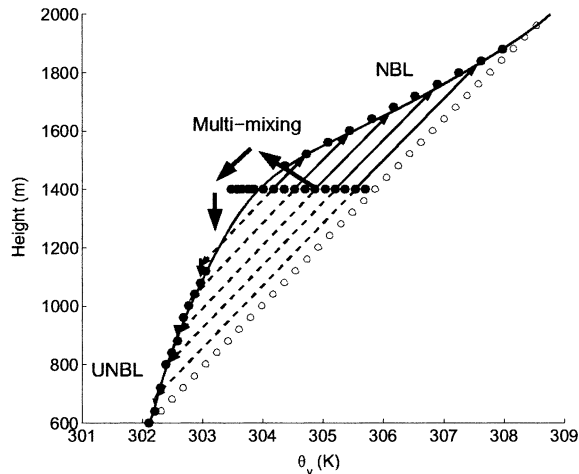


FIG. 3. An illustration of the treatment of positively buoyant mixtures under NBL, UNBL, and multimixing. (solid line) The environmental  $\theta_v$  sounding. (open circles) The ascent of USCA. (filled circles) A mixture spectrum generated at 1400 m. (solid arrows) The moist adiabatic ascent to mixtures' NBL (RB86). (dashed arrow) The adiabatic descent to mixtures' UNBL (E91). (thick arrows) The multi-mixing treatment of positively buoyant mixtures.

mixing, preserve large amounts of liquid water when reaching their inversion-level NBL. Compared to the drier mixtures 1 and 2, mixtures 3 and 4 have much larger  $\theta_i$  and  $q_i$  differences relative to the environment. Figures 2a and 2b show this divergence of  $\theta_i$  and  $q_i$  values above the inversion. However, liquid water-containing mixtures such as 3 and 4 presumably do not remain neutrally buoyant when further mixing and evaporation occurs. Evaporative cooling may drive them downward; the UNBL detrainment criterion accounts for this effect by detaining these mixtures at lower levels (Figs. 2d–f). For mixture 3, UNBL detrainment occurs 400 m below its initial NBL. This further descent seeks the level where cloudy air ultimately detains and is therefore physically more plausible; we adopt the UNBL detrainment criterion for negatively buoyant mixtures below.

As Fig. 2 shows, the two detrainment criteria differ sharply in their treatment of positively buoyant mixtures. Given the UNBL detrainment criterion and an unsaturated environment for which  $\theta_{iv} = \theta_v$  increases monotonically with height, all nonprecipitating cloud mixtures at level  $i$  satisfy  $\theta_{iv}^{i,j} \leq \theta_{iv}^i$  and will descend. In particular, positively buoyant mixtures with their larger liquid water contents often detrain well below the mixing level due to strong evaporative cooling. These same positively buoyant mixtures, given the NBL detrainment criterion, produce updrafts rather than downdrafts, and account for significant transport into the inversion layer.

Figure 3, which is similar to Fig. 1c but retains only a single mixture spectrum at 1400 m, shows schematically the difference between the treatment of positively buoyant mixtures under NBL, UNBL, and multimixing

detrainment described below. The initially generated mixing spectrum (at the 1400-m level) is separated into mixtures that are neutrally or negatively buoyant (black circles to the left of the environmental  $\theta_v$  sounding) or positively buoyant (with  $\theta_v^{i,j} > \theta_v$ ). Notice that the relatively undilute positively buoyant mixtures either ascend adiabatically to near cloud top and detrain under NBL detrainment, or descend adiabatically to near cloud base and detrain under UNBL detrainment (the UNBL levels are not necessarily the intersection level of the mixtures moist adiabat and the environmental sounding). Given fixed amount of USCA, the convective upward mass flux and its associated  $\theta_i$  and  $q_i$  transport are significantly reduced by detrainment at the UNBL, compared with NBL detrainment.

In the shedding thermal model, positively buoyant cloudy mixtures deposited in the wake of the ascending thermals must undergo further mixing. These mixtures should be diluted and detrain somewhere between the NBL and the UNBL of the initial mixture, as illustrated in Fig. 3. We introduce a simple form of multimixing in section 2e and appendix B, in which positively buoyant mixtures are mixed on their way toward their NBL. For simplicity, after each mixing event the positively buoyant mixtures are grouped and averaged into a single updraft parcel, continue ascending to the next higher level and pursue further mixing until further mixing generates only neutrally and/or negatively buoyant mixtures. During this process only neutrally and negatively buoyant mixtures are detrainment. The detrainment levels are chosen to be the mixtures' UNBL; that is, this detrainment criterion is UNBL detrainment limited to neutrally and negatively buoyant mixtures. The addition of multimixing accounts for the further mixing of the active cloudy parcels. As a result, the total amount of entrained environmental air is increased, and model-produced mixtures are not solely mixtures between USCA and the environment. We use this modified detrainment criterion in our diagnosis of the UER in section 2e below.

#### d. Mixing distributions

There is little observational or laboratory evidence to constrain the mixing distribution  $P(\sigma^j)$  required by (3). In Fig. 4 we present four distributions that have been discussed in the context of EMBS parameterizations. Shown are distributions of eroded USCA ( $u$ ), environmental air ( $e$ ), and their sum ( $u + e$ ) as a function of environmental fraction  $\sigma$ . The curves are normalized so that the total  $u$  in the spectrum is unity. Distributions P1 and P2 make two different assumptions about uniform mixing. E91 (P1) assumes a fixed amount of USCA in each mixture, with more environmental air entrained into mixtures with larger  $\sigma^j$ . RB86 (P2) assume a uniform probability of formation of mixing fractions, so that the resulting total mass flux (environment plus USCA) of each mixture is constant, and parcels with a higher environmental mass fraction  $\sigma^j$  contain less sub-cloud air.

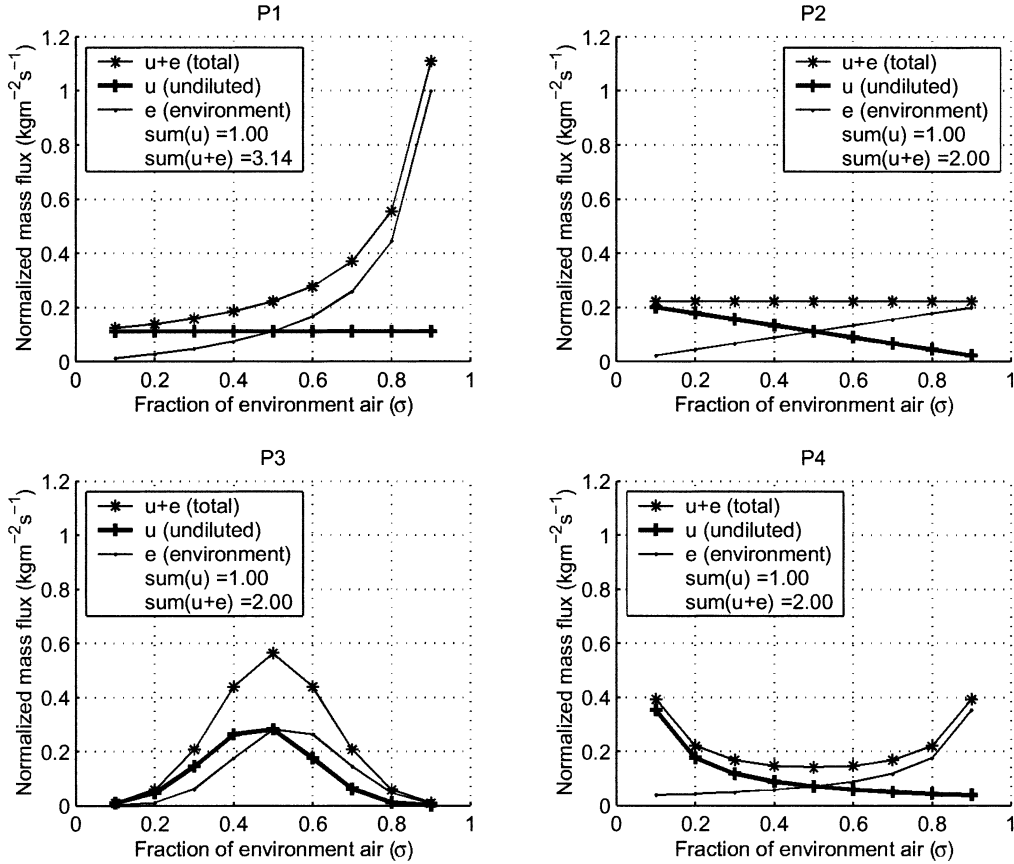


FIG. 4. Mixing distributions as a function of environmental air fraction  $\sigma$  for a selection of EMBS models: P1 is from E91 [Eq. (7)]; P2 is from RB86; P3 is from Kain and Fritsch (1990); P4 is determined following Cohen (2000).

Kain and Fritsch (1990) assume that cumulus turbulence tends to mix USCA and environment air in equal portions, and apply a Gaussian distribution centered at  $\sigma = 50\%$  with standard deviation given as 0.2 (hereafter called P3). Recently, Cohen (2000) suggested an anti-Gaussian distribution of cloud mixtures based on his numerical simulation of cumulonimbus clouds. Distribution P4 is an analytic function that approximates the shape of Cohen's mixture distribution. The four normalized distributions of USCA (given by the thick line in Fig. 4) are

$$P1(\sigma^j) = \frac{1}{N}, \quad (5a)$$

$$P2(\sigma^j) = \frac{(1 - \sigma^j)}{\sum_{j=1}^N (1 - \sigma^j)}, \quad (5b)$$

$$P3(\sigma^j) = (1 - \sigma^j)G(\sigma^j), \quad \text{and} \quad (5c)$$

$$P4(\sigma^j) = \frac{(1/\sigma^j)}{\sum_{j=1}^N (1/\sigma^j)}, \quad (5d)$$

where  $G(\sigma^j)$  is a Gaussian distribution with mean = 0.5 and standard deviation = 0.2. Note from Fig. 4 that the total amount of entrained environmental air is larger in distribution P1 than in distributions P2–P4. Below we use  $N = 81$  with  $\sigma^j$  equally spaced within the range  $0.1 \leq \sigma^j \leq 0.9$ . The model results below are not sensitive to the specified number of mixtures, and resolutions of  $N \approx 10$ –20 give similar results. In section 3e, we test the sensitivity of the EMBS to each of these distributions.

#### e. Diagnostic equations for the UER

Given  $P(\sigma^j)$  and a detrainment criterion, the final specification required by an EMBS is the UER as a function of vertical level. Parameterization of the UER is a major unresolved problem for EMBS models (e.g., Emanuel and Zivkovic-Rothman 1999, hereafter EZ99). The difficulty is magnified when these models are used to represent an ensemble of clouds, because observations show that cumulus cloud fields are characterized by a range of cloud heights and sizes (e.g., Plank 1969). Our approach in this section is to derive a UER profile

that is consistent with an observed equilibrium state and large-scale forcings for shallow cumulus convection. We develop a discretized version of (1) which, for nonprecipitating clouds, is linear in the UER and can therefore be solved given an equilibrium atmosphere. The discretization includes a treatment of simplified multimixing for positively buoyant mixtures as outlined in section 2c.

At any level  $i$  between cloud base and cloud top (ICB  $\leq i \leq$  ICT), the total eroded USCA mass flux is represented by  $U^i$ . The mass flux of an individual mixture  $j$  involved with mixing with part of the eroded  $U^i$  is determined by (4), which we rewrite as

$$m^{i,j} = \frac{P(\sigma^j)}{1 - \sigma^j} U^i = X^j U^i. \quad (6)$$

If  $m^{i,j}$  is neutrally or negatively buoyant with respect to its environment ( $\theta_v^{i,j} \leq \theta_v^i$ ), we detrain it by finding its detrainment level  $k$  ( $k \leq i$ ) based on  $\theta_v^{i,j} = \theta_v^k$  (i.e., the UNBL). Knowing the detrainment level  $k$ , we can find the mass flux contribution of the mixture  $m^{i,j}$  to any model level  $n$ :

$$\text{MFX}^{n,i,j} = \begin{cases} 0 & n > i \\ -m^{i,j} = -X^j U^i & k < n \leq i \\ 0 & n \leq k \\ 0 & n = k = i. \end{cases}$$

The detrainment contributions of  $m^{i,j}$  to the environmental  $\theta_i$ ,  $q_i$ , at any level  $n$  are

$$\text{DTL}^{n,i,j} = \begin{cases} (\theta_i^{i,j} - \theta_i^k) m^{i,j} = (\theta_i^{i,j} - \theta_i^k) X^j U^i & n = k \\ 0 & n \neq k \end{cases}$$

$$\text{DQT}^{n,i,j} = \begin{cases} (q_i^{i,j} - q_i^k) m^{i,j} = (q_i^{i,j} - q_i^k) X^j U^i & n = k \\ 0 & n \neq k. \end{cases}$$

We sum over the set  $\{j\}$  of all mixtures that are negatively or neutrally buoyant to obtain the total mass flux and detrainment contributions at level  $n$  caused by the USCA mixing event at level  $i$ :

$$\sum_{\{j\}} \text{MFX}^{n,i,j} = \text{MF}^{n,i} U^i, \quad (7a)$$

$$\sum_{\{j\}} \text{DTL}^{n,i,j} = \text{DT}^{n,i} U^i, \quad \text{and} \quad (7b)$$

$$\sum_{\{j\}} \text{DQT}^{n,i,j} = \text{DQ}^{n,i} U^i, \quad (7c)$$

where  $\text{MF}^{n,i}$ ,  $\text{DT}^{n,i}$ , and  $\text{DQ}^{n,i}$  represent, respectively, the  $U^i$ -normalized total mass flux and detrained  $\theta_i$  and  $q_i$  tendencies at level  $n$  due to the mixing of USCA at level  $i$ . Both the mixing-induced mass flux and the detrained tendencies are linear functions of  $U^i$ .

The treatment of the set  $\{j'\}$  of all mixtures that are positively buoyant ( $\theta_v^{i,j'} > \theta_v^i$ ) is described in appendix B. To summarize, the average  $\theta_i$  and  $q_i$  of set,  $\{j'\}$  is calculated. The mixtures are grouped into a single parcel and carried to the next higher level. New mixtures are

generated; positively buoyant mixtures continue to merge, ascend, and mix, while other mixtures are detrained. This process continues until new mixtures are all neutrally or negatively buoyant mixtures and subsequently are detrained. Multimixing completes the mixing and detrainment of a single convective element  $U^i$ , which is eroded at level  $i$ . Without multimixing, the detrainment relationships of (7) can be reduced to those of either RB86 or E91, given appropriate choices for the detrainment level  $k$ .

This algorithm is carried out for all levels  $i$  (ICB  $\leq i \leq$  ICT) and produces three two-dimensional arrays:  $\text{MF}^{n,i}$ ,  $\text{DT}^{n,i}$ , and  $\text{DQ}^{n,i}$ . Thus, assuming an equilibrium atmosphere, a discretized version of (1) may be formulated as

$$-g \left( \frac{\Delta \theta_i}{\Delta p} \right)^n \left[ \sum_{i=n+1}^{\text{ICT}} U^i + \sum_{i=\text{ICB}}^{\text{ICT}} \text{MF}^{n,i} U^i \right] + \frac{g}{\Delta p} \sum_{i=\text{ICB}}^{\text{ICT}} \text{DT}^{n,i} U^i = \phi_T^n \quad (8a)$$

$$-g \left( \frac{\Delta q_i}{\Delta p} \right)^n \left[ \sum_{i=n+1}^{\text{ICT}} U^i + \sum_{i=\text{ICB}}^{\text{ICT}} \text{MF}^{n,i} U^i \right] + \frac{g}{\Delta p} \sum_{i=\text{ICB}}^{\text{ICT}} \text{DQ}^{n,i} U^i = \phi_q^n, \quad (8b)$$

where  $\phi_T^n$  and  $\phi_q^n$  represent the sum of all large-scale forcings of environmental  $\theta_i$  and  $q_i$ , respectively. Inserting (7) into (8), we find two sets of linear equations for  $U$ . Given the large-scale forcings ( $\phi_T^n$  and  $\phi_q^n$ ) and mixing distribution  $P(\sigma^j)$ , (8a) and (8b) may be solved either independently or as a coupled system. Having obtained the  $U$  profile, the UER profile is simply  $E = U/\Delta z$ . We show in appendix C that, for BOMEX forcings, independent solutions of (8a) and (8b) give consistent solutions of the UER profile. In the diagnosis of section 3, we simply retrieve the UER by (8a), followed by smoothing using a three-point running mean. The smoothed UER is then substituted into (8a) and (8b) to verify that the residual tendencies are small compared to the uncertainties of the data. We discuss the details of the inversion technique, the consistency, and stability of the solutions in appendix C.

Figure 5 summarizes episodic mixing and buoyancy sorting as calculated using the framework described above and in appendix B. The left-hand side of Fig. 5 illustrates the ascent of USCA from cloud base to cloud top (the cloud-base height and cloud-top height are determined, respectively, by the LCL and the NBL of the USCA at the upper surface layer). This is an idealized representation of nonlocal transport such as the shedding thermal model discussed in section 1. The small cutout in the left-hand side shows a single ‘‘convective element’’ of USCA, which is eroded at vertical level  $i$ .

In the right-hand side of Fig. 5 we show initial and subsequent mixing events between this eroded USCA

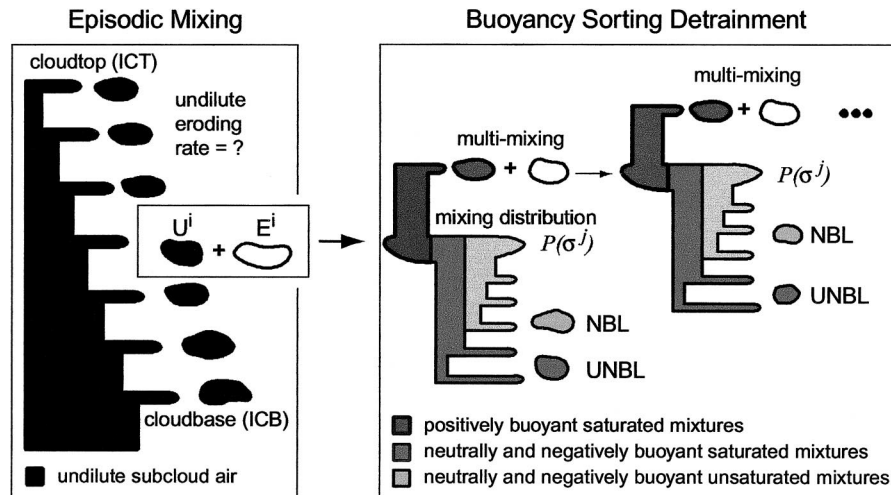


FIG. 5. An illustration of the episodic mixing and buoyancy sorting model. (left) The episodic mixing process between USCA (black) and environment (white). The small cutout on the left illustrates the mixing with the environment of a single convective element  $U^i$  at level  $i$ . (right) The buoyancy sorting process, showing initial and secondary mixing given mixing distribution  $P(\sigma^j)$ , with detrainment of neutrally and negatively buoyant mixtures at their NBL (unsaturated) or UNBL (saturated). The three dots in the upper right-hand corner indicate further mixing events, which continue until there are no positively buoyant mixtures.

element  $U^i$  and the environment. We distinguish between the remaining positively buoyant USCA and positively buoyant mixtures, which experience more efficient dilution and therefore can only ascend a short distance from their mixing level depending on their average buoyancy. We specify the same mixing distribution  $P(\sigma)$  for both the initial and subsequent mixing events, and test the sensitivity of the model to the mixing distribution in section 3e, below. The positively buoyant mixtures are always homogenized and undergo further ascent and mixing until all new mixtures are neutrally or negatively buoyant and are detrainment at their NBL (unsaturated mixtures) or UNBL (saturated mixtures). Applying the UNBL detrainment criterion enforces the complete evaporation of saturated mixtures before their final detrainment. The multimixing treatment of positively buoyant mixtures accounts for the further mixing and dilution of cloudy turbulent wake in the shedding thermal model, permits the existence of upward-moving mixtures, and eliminates the deep penetrative downdrafts otherwise caused by detrainment of positively buoyant mixtures at their UNBL.

### 3. Results

In this section we apply the diagnostic UER retrieval of (8) to equilibrium shallow cumulus convection. We use vertical sounding and forcing profiles taken from the Global Energy and Water Cycle Experiment (GEWEX) Cloud Systems Study (CSS) BOMEX intercomparison, which provides a prescribed large-scale subsidence rate and rates for radiative cooling and subcloud-layer advective drying (Siebesma and Cuijpers

1995; Siebesma et al. 2003). The forcing data is consistent with BOMEX phase III (22–26 June 1969), which provides a 4-day period during which the non-precipitating trade cumulus boundary layer was in steady state, with the large-scale advective and radiative forcings in balance with the cloud response. Although idealized, the BOMEX case study insures a consistent set of large-scale forcings with which an equilibrium state for a shallow cumulus cloud boundary layer is established in large eddy simulations. The model-produced equilibrium vertical profiles of temperature and moisture closely match the observed BOMEX atmosphere (Nitta and Esbensen 1974; Siebesma and Cuijpers 1995; Siebesma and Holtslag 1996). In section 3b we present the UER retrieval together with vertical profiles for mass flux  $M_f$  and the lateral detrainment of total water.

#### a. Large-scale environment

Figures 6a,b show the horizontally averaged vertical profiles of the BOMEX equilibrium LES output for  $\theta_i$  and  $q_i$  (Siebesma and Cuijpers 1995; Siebesma et al. 2003). The figure shows the typical layer structure for shallow cumulus convection: a well-mixed subcloud layer between approximately 0 and 500 m, a conditionally unstable cloud layer between 500 and 1500 m, and an overlying inversion layer.

Figures 6c,d shows the large-scale forcings of  $\theta_i$  and  $q_i$  calculated based on the specified large-scale subsidence, radiative cooling, and subcloud-layer advection. Given the observed equilibrium state, we expect that the cloud response will balance the net large-scale forc-

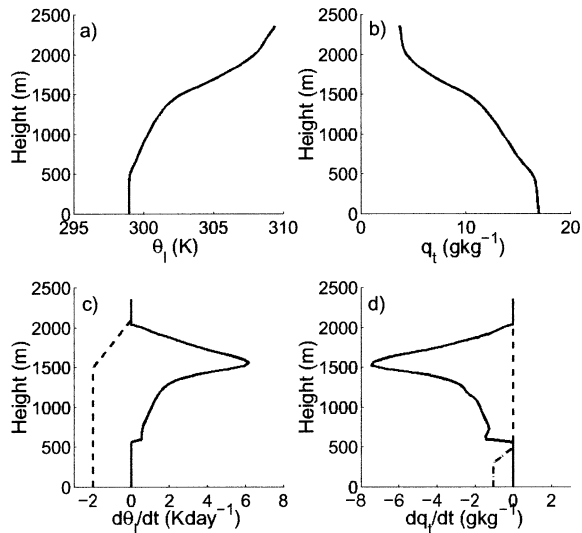


FIG. 6. BOMEX equilibrium state. (a) Liquid water potential temperature  $\theta_l$ . (b) Total water specific humidity  $q_t$ . (c) Solid line is  $\theta_l$  tendency due to subsidence:  $\rho g w (\partial \theta_l / \partial p)$ ; dashed line is radiative cooling:  $-Q_R$ . (d) Solid line is  $q_t$  tendency due to subsidence:  $\rho g w (\partial q_t / \partial p)$ ; dashed line is large-scale advective drying:  $-\mathbf{V}_H \cdot \nabla q_t$ .

ing throughout the cloud layer and the inversion layer. As indicated in Figs. 6c,d the cloud ensemble must cool and moisten the inversion layer and upper cloud layer, and slightly heat and moisten the lower cloud layer.

### b. UER retrieval

We use the diagnostic approach described by (8) to retrieve the UER given the equilibrium soundings shown in Fig. 6. For this retrieval, we follow E91 and assume mixing distribution P1, so that at each model level  $U^i$  is equally divided and then mixed with different proportions of environment air.

Figure 7 shows the diagnosed results. Figure 7a presents the UER retrieved by solving (8a) for the forcings of Fig. 6c. Within the cloud layer, the UER decreases exponentially with increasing height. Near the bottom of the inversion, it increases before decreasing almost linearly throughout the inversion layer. As shown in Fig. 7c (dotted line), with the diagnosed UER, the EMBS model produces a cumulus-induced  $\theta_l$  tendency that balances the large-scale  $\theta_l$  tendency. As a consistency check, the retrieved UER is put back into the EMBS model; Fig. 7d (dotted line) shows the resulting net  $q_t$  tendency. Exact balance for the  $q_t$  tendency is not expected, given uncertainties in the specified sounding and forcing data; however, the net  $q_t$  tendency in Fig. 7d is within the range of the residual LES tendencies (P. Siebesma 2002, personal communication; available online at <http://www.knmi.nl/siebesma/gcss/tend3d.html>). In appendix C, we present additional results showing the consistency of the  $\theta_l$ ,  $q_t$  retrievals.

Figure 7b shows the mass flux calculated using the diagnosed UER, partitioned into undilute ascending up-

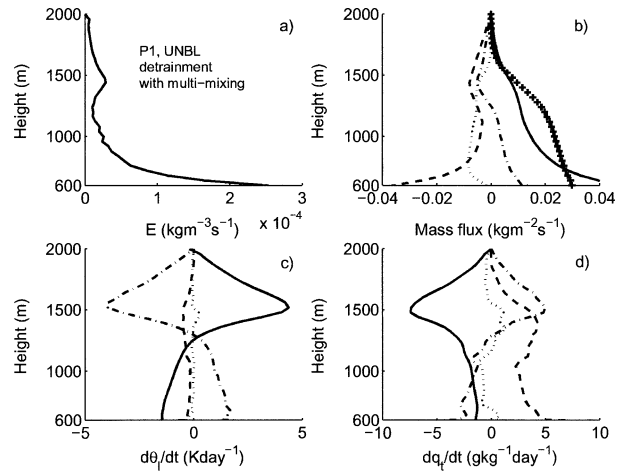


FIG. 7. Diagnosed fluxes and tendencies from the EMBS model. (a) UER retrieved by solving (8a). (b) Solid line is upward mass flux due to ascending USCA; dashed line is downward mass flux due to descent of initially negatively buoyant mixtures; dotted line is net mass flux produced by initially positively buoyant mixtures through multi-mixing; dotted-dashed line is the total net mass flux produced by the EMBS model; crosses are the cloud mass flux obtained from an LES case study. (c) Solid line is total large-scale forcing of  $\theta_l$ ; dotted-dashed line is induced  $\theta_l$  tendency due to cloud net mass flux; dashed line is cloud lateral detrained tendency; dotted line is the total net tendency. (d) As in (c), but for total water specific humidity  $q_t$ .

drafts (solid line), downdrafts induced by initially negatively buoyant mixtures (dashed line), and downdrafts induced by initially positively buoyant mixtures through multimixing (dotted line). The cloud net mass flux is given by the dotted-dashed line, while the line marked by crosses shows the net cloud mass flux from the liquid water-containing grid cells of the BOMEX LES (Siebesma and Cuijpers 1995; Siebesma et al. 2003).

The net mass flux from the LES is significantly larger than the EMBS-diagnosed profile, which is downward within the inversion layer and upward below the inversion. For the EMBS model, the vertical integral of the  $\theta_l$  tendency induced by the net cloud mass flux is close to zero, consistent with the fact that nonprecipitating clouds only transport  $\theta_l$ , and do not act as net sources or sinks of  $\theta_l$ . This disparity between the LES and EMBS-produced mass flux is due in part to their different definitions of the cumulus cloud boundary. Recall that the UNBL detrainment criterion, which defines the cloud boundary to include a surrounding region of unsaturated air, incorporates cloud evaporation and the associated unsaturated convective downdrafts into the net cloud mass flux. In the LES, in contrast, clouds are defined as saturated cloudy parcels that have liquid water. Indeed, in Fig. 7c, we see little lateral detrained  $\theta_l$  tendency (dashed line) while the detrained water vapor tendency is still significant in Fig. 7d (dashed line), as parcels reach their UNBL with a small  $\theta_l$  deficit but with larger excess  $q_t$ . (See Figs. 2d and 2e, where detrained  $q_t$  differences are larger than  $\theta_l$  differences.)

An additional feature of the partitioned EMBS mass

flux apparent in Fig. 7b is the counterintuitive fact that, in this EMBS model, positively buoyant mixtures produce a net downward mass flux (dotted line). This downward motion is due to the evaporation of liquid water in these mixtures via two processes, as illustrated in Fig. 3. One is explicit mixing with environmental air and the generation of new mixture spectra; the other is the moist adiabatic descent of saturated, negatively buoyant mixtures prior to their detrainment. Both occur before the final detrainment of cloud-processed air to the environment at the equilibrium level (UNBL). As a result, all liquid water evaporation is realized within clouds and the absorbed latent heat cools the cloud air itself, rather than directly cooling the environment. This evaporative cooling drives cloud air parcels downward. Thus, the cloud evaporative cooling of the environment is represented through the net downward mass flux, rather than through the direct local detrainment of liquid water. In reality, much of this evaporation occurs at the dissipation stage and is characterized by a significant number of unsaturated downdrafts. Given this life cycle perspective, the EMBS models (with UNBL detrainment) can be understood as a simple representation of the two stages of a cumulus life cycle: growth, incorporated through the ascent of USCA, and dissipation, represented by the mixing, evaporation, and detrainment of both the USCA and the initially positively buoyant mixtures.

### c. Linking the UER to the cloud size distribution

Parameterization of the UER profile remains a difficult issue for EMBS models. In RB86, the UER is taken to be constant with height, an assumption that distributes the undilute cloud-base mass flux equally into each of the model levels. A second approach has been adopted by EZ99 and is motivated by the two-dimensional single cloud simulation of Bretherton and Smolarkiewicz (1989). Based on the model results, the EZ99 UER parameterization takes the UER to be a function of the vertical gradient of buoyancy in clouds. Specifically,  $E^i$ , normalized by the cloud layer-averaged UER  $E_0$ , is

$$\frac{E^i}{E_0} = \frac{H}{\Delta z} \left( \frac{(|\Delta B| + \Lambda \Delta p)^i}{\sum_{j=ICB}^{ICT} (|\Delta B| + \Lambda \Delta p)^j} \right), \quad (9)$$

where  $H$  is the cloud layer depth,  $E_0 = (1/H) \sum_{i=ICB}^{ICT} E^i \Delta z$ ,  $\Lambda$  is a constant mixing parameter ( $0.06 \text{ mb}^{-1}$ ),  $B$  is the buoyancy of the ascending USCA, and  $\Delta B$  is the change in undilute buoyancy over a pressure interval  $\Delta p$ . Note that  $(H E_0)$  is the undilute cloud-base mass flux  $F^b$ , and  $(\Delta z E^i)$  is the eroded USCA mass flux  $U^i$ .

Figure 8a shows  $E/E_0$  for the BOMEX soundings based on both RB86 and EZ99. The retrieved UER from Fig. 7a is replotted in Fig. 8b for comparison. Both the retrieval and the EZ99 parameterization show a small

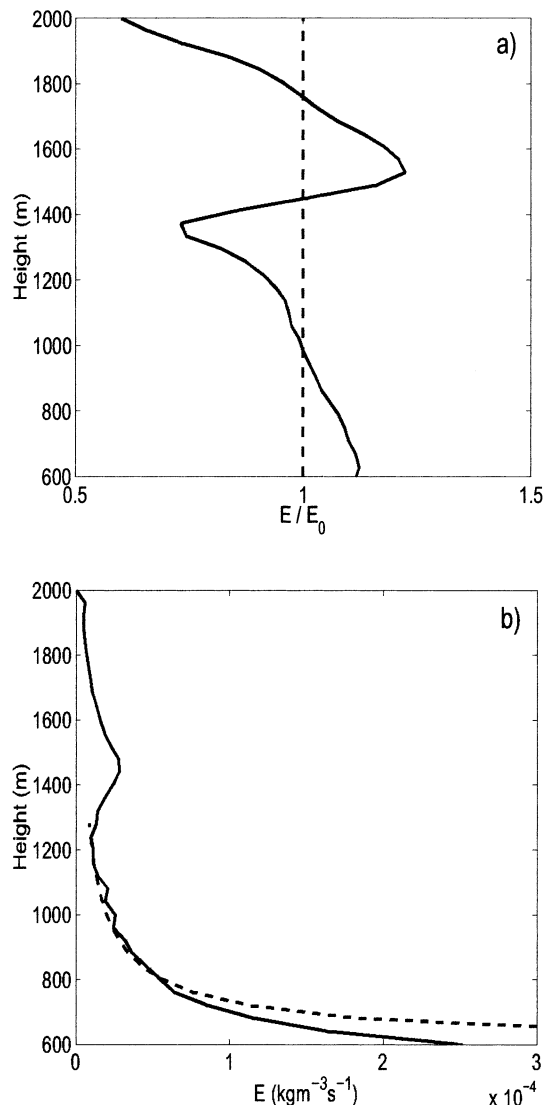


FIG. 8. (a) UER  $E$  normalized by average  $E_0$  for BOMEX cumuli following RB86 (dashed line) and EZ99 (solid line). (b) A comparison of the diagnosed UER (solid line) and a cloud size/height distribution from shallow cumuli (dashed line).

increase in the UER near the base of the inversion at approximately 1400 m. In contrast, in the cloud layer, the retrieved UER decreases exponentially from cloud base to the inversion base.

Given that the equilibrium soundings of Figs. 6a,b are the cumulative product of a size-distributed cloud population, we compare the retrieved UER in Fig. 8b with a shallow cumulus cloud size distribution calculated from LES results by Neggers et al. (2003). This distribution has a power-law form that is typical of several studies of shallow cumulus size distributions (e.g., Cahalan and Joseph 1989; Kuo et al. 1993; Benner and Curry 1998). This size/height distribution for clouds with diameters less than  $\approx 1$  km is given by

$$N(h) = a(h - h_b)^b, \quad (10)$$

where  $b = -1.7$ ,  $h_b$  is cloud-base height (600 m for BOMEX),  $h$  is cloud-top height, and  $h - h_b$  is cloud depth or cloud size. Here,  $a$  is a free scaling parameter. We have transformed (10) from cloud horizontal size to cloud height assuming an aspect ratio of 1 (see, e.g., Betts 1973).

In Fig. 8b we compare the retrieved UER and the normalized cloud height/size distribution for small-to medium-sized clouds (thicknesses  $< 1$  km). Both profiles first rapidly decay near cloud base and then steadily decrease with increasing cloud height/size. In section 3d, we examine the  $d\theta_i/dt$  and  $dq_i/dt$  profiles determined by the EMBS model applied to single clouds of varying sizes, and show that the retrieved UER profile from an ensemble of clouds in Fig. 8b is qualitatively consistent with the superimposed effect of individual clouds with a size distribution determined by (10). The EZ99 model produces increased erosion of USCA for clouds with thicknesses greater than 1 km, due to the sudden change in stability in the vicinity of the inversion (Fig. 8a). The EMBS-retrieved UER displays a corresponding  $E$  increase in Fig. 8b.

#### d. Single cloud and cloud ensemble effects

Given the fact that a shallow cumulus boundary layer consists of a broad range of cloud sizes, we next examine the total convective effect [i.e., the sum of terms I and II in (1)], for four clouds with respective thicknesses of 1400, 900, 400, and 200 m. For each of these clouds, we calculate the tendencies  $d\theta_i/dt$  and  $dq_i/dt$  using the EMBS model described in section 2e, with constant UER and the mixing distribution P1. The assumption of a constant UER for individual clouds is supported by the two-dimensional numerical simulation of Bretherton and Smolarkiewicz (1989), which indicates that the entrainment of environmental air is relatively uniform, while detrainment can occur at preferential levels. A constant UER has also been used by RB86 to successfully reproduce the observed cloud height, mass flux, and cloud detrainment in individual nonprecipitating cumulus clouds.

We take the cloud-base mass flux to be a linear function of cloud thickness  $\Delta h$  (RB86):

$$F^b = \chi \Delta h, \quad (11)$$

where  $\chi$  is chosen to be  $1.25 \times 10^{-5} \text{ kg m}^{-3} \text{ s}^{-1}$ . This  $\chi$  value produces net cooling and moistening tendencies at the inversion that are roughly equal to the forcing at that level for the 1400-m-thick cloud. Scaling  $F^b$  by the cloud thickness is consistent with the idea that deeper clouds need larger quantities of USCA to reach higher into the upper environment.

Figure 9 shows the convective tendencies for the four individual clouds. We see that the two thickest clouds produce roughly symmetric cooling and moistening near their cloud top and warming and drying near their cloud base. For the 400-m-thick cloud, moistening and cooling

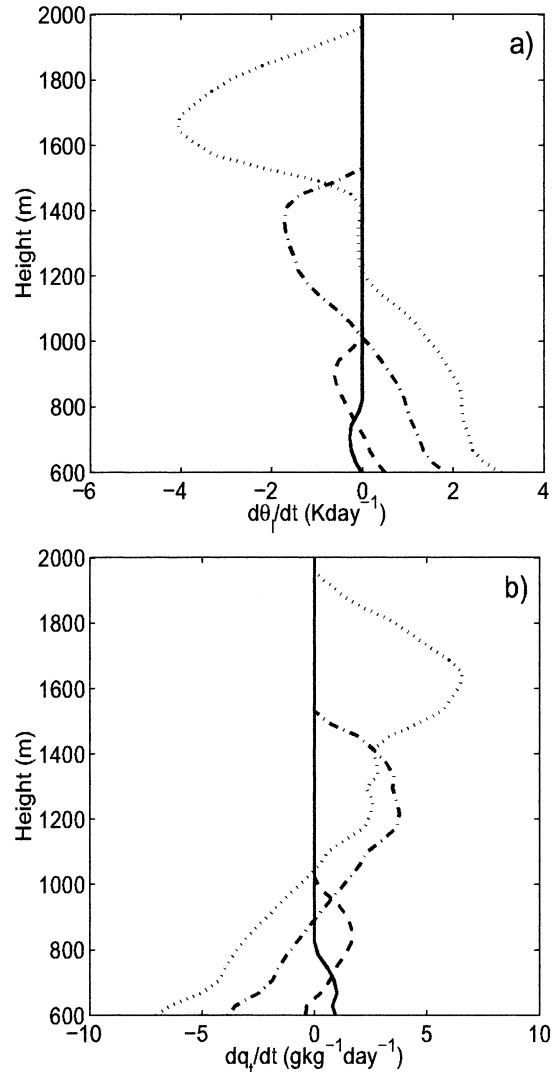


FIG. 9. Single cloud-induced net tendencies of entropy and total water specific humidity [sum of terms I and II of (1) calculated from an EMBS]. (a)  $\theta_i$  tendencies due to individual clouds of different size; dotted line is large cloud (thickness  $\Delta h = 1400$  m); dotted-dash line is medium cloud ( $\Delta h = 900$  m); dashed line is small cloud ( $\Delta h = 400$  m); solid line is smallest cloud ( $\Delta h = 200$  m). (b) As in (a), but for  $q_i$  tendencies.

tends to dominate most of the cloud depth except near its base. The smallest cloud cools and moistens the environment throughout its depth.

Figure 10 shows the decomposed tendencies as in Fig. 7c,d, but for the single 1400-m-thick cloud. We see most of the cooling and moistening near the cloud top is due to the cloud downdraft-induced environmental compensating upward motion, while most of the warming and drying near the cloud base is due to the cloud updraft-induced environmental compensating subsidence. As in Fig. 7c, the cloud detrained temperature tendency is close to 0. The cloud detrained water tendency is significant throughout most of the cloud layer, with a max-

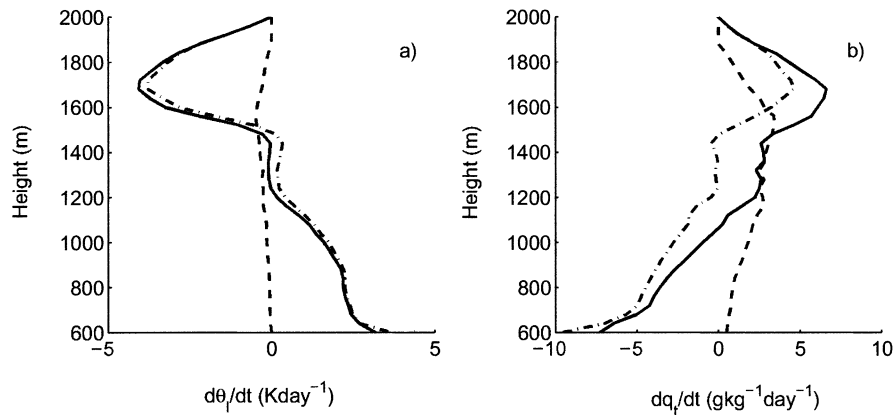


FIG. 10. Decomposed tendencies for the 1400-m-deep cloud of Fig. 9. (a) Dotted-dashed line is induced  $\theta$ , tendency due to cloud net mass flux; dashed line is cloud lateral detrained tendency; solid line is the total net tendency. (b) As in (a), but for total water specific humidity  $q_t$ .

imum near the base of the inversion layer. The cloud-top cooling and moistening is not concentrated in a single layer at cloud top, as would be expected with an entraining plume model. Instead it extends to roughly half the cloud depth, gradually decreasing to zero.

In contrast with the two thickest clouds, the vertical tendency profiles for the two smallest clouds in Fig. 9 are dominated by moistening and cooling. This is due to the fact that many cloud-top mixtures seek their UNBL detrainment level at cloud base for these cases. This produces a downward net mass flux throughout the smallest cloud, with corresponding induced upward motion in the environment. This result is consistent with observations from the Small Cumulus Microphysics Study (SCMS) that show that while large clouds transport net mass upward, small clouds (depth  $< 350$  m) have average downward transport, while accounting for 50% of the cloud cover (Duykerke 1998). Since the USCA ( $\theta_i$ ,  $q_i$ ) is slightly cooler and moister than the cloud-base environment, the cooling and moistening is distributed approximately uniformly within the very shallow cloud depth.

In general, the convective tendencies produced by the EMBS model for individual clouds of different thicknesses are consistent with the results of Esbensen (1978). Esbensen (1978) used a laterally entraining plume model to represent clouds that penetrate into the inversion, combined with a bulk model of shallower cloud circulations below the inversion base. He found that the deep clouds are primarily responsible for the warming and drying of the lower cloud layer, while the shallower clouds are primarily responsible for moistening below the inversion base.

Comparing Fig. 9 with the total forcing shown in Fig. 6, it is apparent that the total forcing requires a cloud response that cools and moistens the inversion layer and upper part of the cloud layer and slightly warms and moistens the lower part of the cloud layer. No single cloud modeled by the simple EMBS assumptions of Fig.

9 can accomplish both these effects. We discuss the contribution of a size-distributed cloud population to the ensemble cloud response in section 4 below.

#### e. Sensitivity tests

In section 3b we retrieved the UER for an equilibrium boundary layer given a particular mixing distribution P1 and the multimixing detrainment criterion. In Fig. 11 we compare the UER retrieved using (8a) for each of the mixing distributions of (5). The retrieved UERs shown in Fig. 11a are nearly identical across mixing distributions P1–P4. Similarly, when each UER is inserted into (8b) and the net  $dq_i/dt$  is calculated, the tendency agreement is essentially independent of the choice of mixing distribution. Thus, provided the EMBS model detrains only neutrally and negatively buoyant mixtures, with positively buoyant mixtures pursuing further mixing, the details of the initial mixing distribution have a very small impact on the convective transport produced by the EMBS parameterization.

To illustrate why the proposed multimixing treatment of positively buoyant mixtures reduces the EMBS model's sensitivity to mixing distribution, we examine a single convective element  $U^i$ , which is brought to a particular level  $i$  and subsequently mixed with the environment. As indicated in the lhs of (8),  $U^i$  influences environmental thermodynamic tendencies in three ways. First, it heats and dries all the levels  $n$  below  $i$  through compensating environmental subsidence caused by its adiabatic ascent. After mixing at level  $i$ , mixtures seek their UNBLs and penetrate specific distances below  $i$ , exiting the cloud given the UNBL detrainment criterion. These penetrative downdrafts cool and moisten their penetrated levels through compensating environmental upward motion. Finally, detrained mixtures also moisten and slightly cool their detrainment levels. The sum of these three tendencies determines the total net tendency at any level  $n$  caused by the ascent, mixing and detrain-

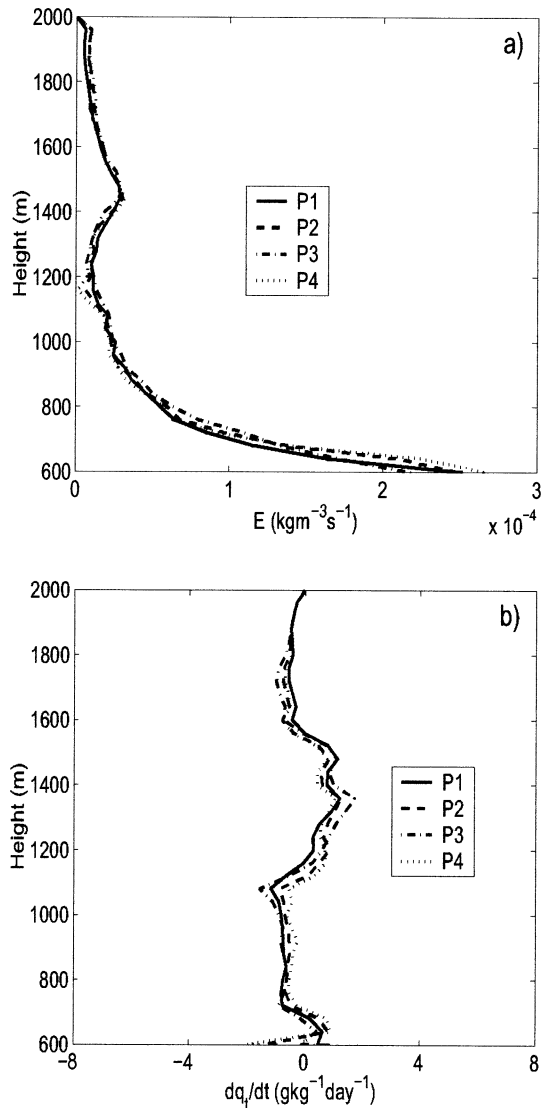


FIG. 11. (a) The retrieved UER based on mixing distributions P1–P4 using (8a). (b) The residual  $q_i$  tendencies calculated from (8b), given the UER of (a).

ment of a particular convective element  $U^i$  and its mixtures.

Figure 12 illustrates the net tendencies and net mass flux induced by a unit USCA ( $U^i = 1 \text{ g m}^{-2} \text{ s}^{-1}$ ) at a particular level  $i$  (1400 m). We have assumed single mixing and the UNBL detrainment criterion for this calculation. First, we see that this particular level's mixing of USCA does not influence any higher levels. This is because, as discussed in section 2c, the UNBL detrainment criterion combined with the single mixing assumption requires that all mixtures detrain below their mixing level for nonprecipitating clouds. Immediately below the mixing level (1400 m) we see a region (about 400 m deep) experiencing net cooling and moistening. This is because most mixtures generated at the mixing level descend and are detrained at levels below 1100

m, and therefore give a net downward motion. This can be seen in the vertical profile of the net mass flux (Fig. 12c) which decreases with height above 600 m and becomes negative at 1100 m, rather than maintaining a constant flux of  $1 \text{ g m}^{-2} \text{ s}^{-1}$ . Between 1000–1100 m, Figs. 12a,b show that the net tendencies change sign from cooling and moistening to heating and drying. This is because the mixtures' downdrafts are not as large as the updrafts of adiabatic ascending USCA. Therefore, the net tendencies are dominated by warming and drying induced by adiabatic ascent. Mixture detrainment also contributes to moistening below the mixing level (not shown).

Figures 12a–c show the tendency and mass flux profiles produced using different mixing distributions. Distribution P1 gives a comparatively concentrated cooling and moistening immediately below the mixing level. This is because P1 entrains more environment air; most P1 mixtures are highly dilute and generate a relatively large but shallow downward mass flux near the mixing level (Fig. 12c). The P2 and P4 distributions have relatively larger proportions of nearly undilute mixtures, which tend to sink long distances and detrain near cloud base (under UNBL detrainment). These mixtures tend to reduce both upper-level cooling and moistening and lower level heating and drying. Distribution P3 has an enhanced proportion of denser, just-saturated mixtures; P3 mixtures tend to cause strong downdrafts concentrated at upper to middle levels (1100–1400 m). Due to their limited liquid water content, they cannot sink as deeply as the positively buoyant mixtures, given UNBL detrainment. Therefore, P4 gives maximum net upward mass flux below 1000 m.

Figure 13 repeats the calculation shown in Fig. 12, with single mixing replaced by the multimixing algorithm described in appendix B. In contrast to Fig. 12, Figs. 13a,b show that the vertical extent and the magnitude of the cooling and moistening is now roughly equal for all mixing distributions, and the transition to heating and drying occurs near 1150–1200 m for P1–P4. Note that the influence of the mixing level now extends above 1400 m, because positively buoyant mixtures are now permitted to ascend. However, the grouping and homogenizing of these mixtures after each mixing event rapidly dilutes the mixtures and limits their region of influence to roughly 150 m above the 1400-m mixing level. The constant upward mass flux (equal to the adiabatic USCA mass flux  $1 \text{ g m}^{-2} \text{ s}^{-1}$ ) below 1100 m shown in Fig. 13c indicates that no mixtures descend below 1100 m for all mixing distributions. Comparison between Fig. 13c and Fig. 12c indicates that the reduction of upward mass flux below 1100 m in Fig. 12c is mainly due to the detrainment of positively buoyant mixtures at their UNBL.

From Fig. 13, we see that multimixing acts to remove the signature of the original mixing distribution by requiring positively buoyant mixtures to undergo additional mixing and detrain at levels higher than their

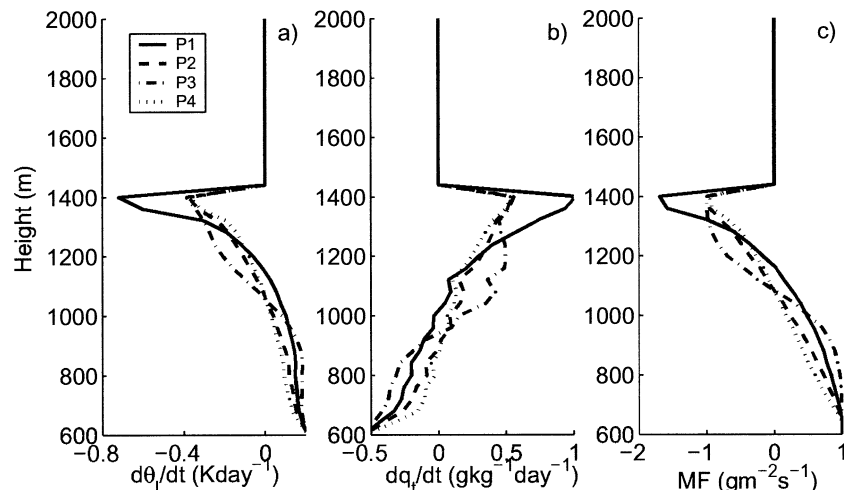


FIG. 12. (a)  $\theta_i$  tendencies computed for the EMBS model using the lhs of (8) for a single convective element  $U^i = 1 \text{ g m}^{-2} \text{ s}^{-1}$  ( $i = 35$ , corresponding to height  $z = 1400 \text{ m}$ ) given single mixing with distributions P1–P4 and the UNBL detrainment criterion. (b) As in (a), but for the  $q_i$  tendencies. (c) Total mass flux due to the ascent, mixing, and detrainment of the  $U^i$  element.

initial UNBL. In contrast to single mixing, multimixing tends to entrain larger quantities of environmental air and produce modified mixing distributions for which dilute mixtures are most probable. Thus, multimixing modifies distributions P2–P4 so that these distributions take on the characteristics of P1, with its large fraction of environmental air and highly dilute mixtures.

We find that the EMBS model is much more sensitive to the choice of detrainment criterion than to the specification of the mixing distribution. Figure 14 repeats the convective element calculation shown in Figs. 12 and 13, substituting NBL detrainment. Under the NBL detrainment criterion, the mixing event at 1400 m significantly cools and moistens the middle inversion layer (1600–1800 m). This is because the positively buoyant mixtures seek their NBL well within the inversion and

produce large detrainment tendencies for both  $\theta_i$  and  $q_i$ . Using Figs. 12, 13, and 14, we can compare the net tendencies caused by the ascent, mixing and detrainment of the single convective element  $U^i$ . We see that, given fixed  $U^i$ , NBL detrainment enhances convective transport, UNBL detrainment reduces convective transport, and transport given multimixing detrainment lies between these two extremes, with more convective cooling and moistening near the mixing level (see Fig. 3).

Figure 15 shows the impact of the detrainment criterion on the entropy and moisture tendencies for all cloud levels with the retrieved  $E$  profile in Fig. 8b and mixing distribution P1. As in the single-level example of Fig. 14, UNBL detrainment gives the smallest convective transport, multimixing gives slightly larger convective transport while NBL detrainment gives the larg-

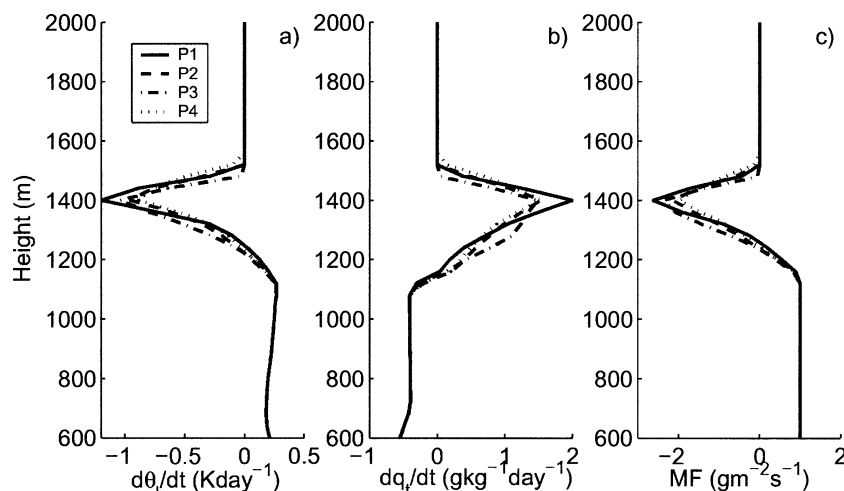


FIG. 13. As in Fig. 12, but using the multimixing algorithm described in appendix B.

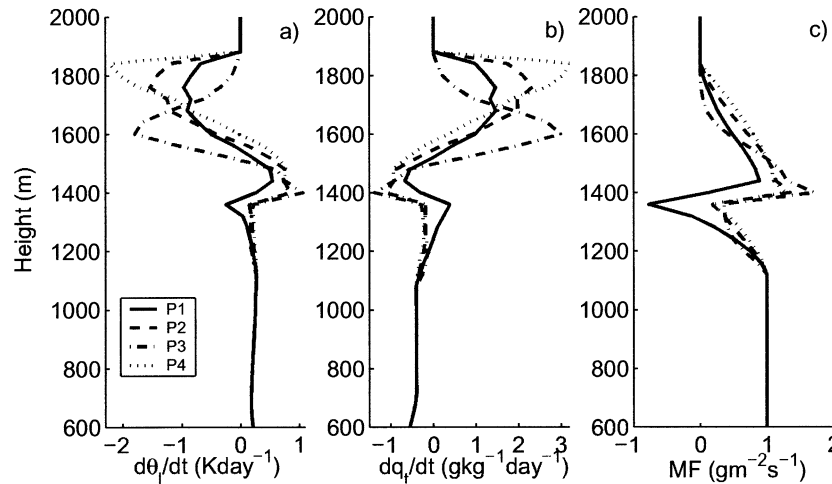


FIG. 14. As in Fig. 12, but using the NBL detrainment criterion.

est convective transport and produces extremely strong cooling and moistening near the top of the inversion. These large cooling and moistening tendencies are due to the fact that nearly all positively buoyant mixtures below the inversion are able to ascend well into the inversion, given the NBL detrainment and the BOMEX sounding as shown in Figs. 2a–c. These positively buoyant mixtures contain large amounts of liquid water and produce extremely large and concentrated cooling and moistening near the top of the inversion. Due to these anomalously large tendencies we find no positive definite vertical profile of the UER that satisfies both (8) and the assumption of direct detrainment at the NBL for the BOMEX case. This leads us to conclude that, at least for the BOMEX case, the UNBL detrainment criterion is more realistic than NBL detrainment for an EMBS model.

#### 4. Discussion

We have applied an EMBS model to an equilibrium sounding of a trade cumulus atmosphere. Our objective is to use the equilibrium constraint and known large-scale forcing to better understand the detailed behavior of this type of model, particularly the impact of undetermined free parameters on the ability of the model to represent the convective transport of shallow clouds. This approach is similar to that of Nitta (1975), who used the spectral entraining plume model of Arakawa and Schubert (1974) to diagnostically determine the contribution of clouds in a particular size range (or equivalently, with a particular entrainment rate) to the total cloud mass flux. A similar approach can be applied to a bulk entraining and detraining plume model, which is often used in shallow cumulus parameterizations.

Bulk entraining and detraining plume models require specification of the vertical profile of the entrainment and detrainment rate. While the entrainment rate might be constrained by laboratory results, the detrainment

parameterization is currently ad hoc, and detrained parcels do not exit the cloud at their NBL, but detrain arbitrarily throughout the layer (Siebesma and Holtslag 1996). The corresponding unknowns for an EMBS model of nonprecipitating clouds are the UER, the detrainment criterion, and the mixing distribution. For a specific choice of mixing distribution and detrainment criterion, we have retrieved a unique vertical profile of the UER, which satisfies an equilibrium constraint. We have investigated the sensitivity of this retrieval to variations in the mixing distribution and the detrainment criterion, and find that, given the requirement that mixtures detrain at their NBL, there is no positive definite vertical UER profile consistent with the observed equilibrium state and the measured large-scale forcings. As discussed in section 3e, this is due to the fact that, for the BOMEX environment, all positively buoyant mixtures ascend into the inversion, where the requirement that they detrain at the NBL produces large updrafts and associated large detrainment of total water and entropy.

Given the alternative assumption of E91—that is, single mixing with all mixtures detrained at their UNBL and mixing distribution P1—it is possible to retrieve a physically plausible profile of the UER. We have introduced a simple form of multimixing to treat positively buoyant mixtures, and with this addition, the EMBS model is nearly insensitive to the choice of mixing distribution. The characteristic UER retrieved via this diagnostic approach is maximum at cloud base, decreasing rapidly through the cloud layer and increasing slightly near the base of the inversion. This vertical structure is consistent with the cloud-base maximum in the entrainment rate diagnosed by Nitta (1975), who argued that the maximum was the product of the large number of small clouds present in the BOMEX boundary layer.

As Fig. 9 shows, an EMBS model applied to the BOMEX environment predicts that, over a range of cloud sizes, individual cumulus clouds cool and moisten

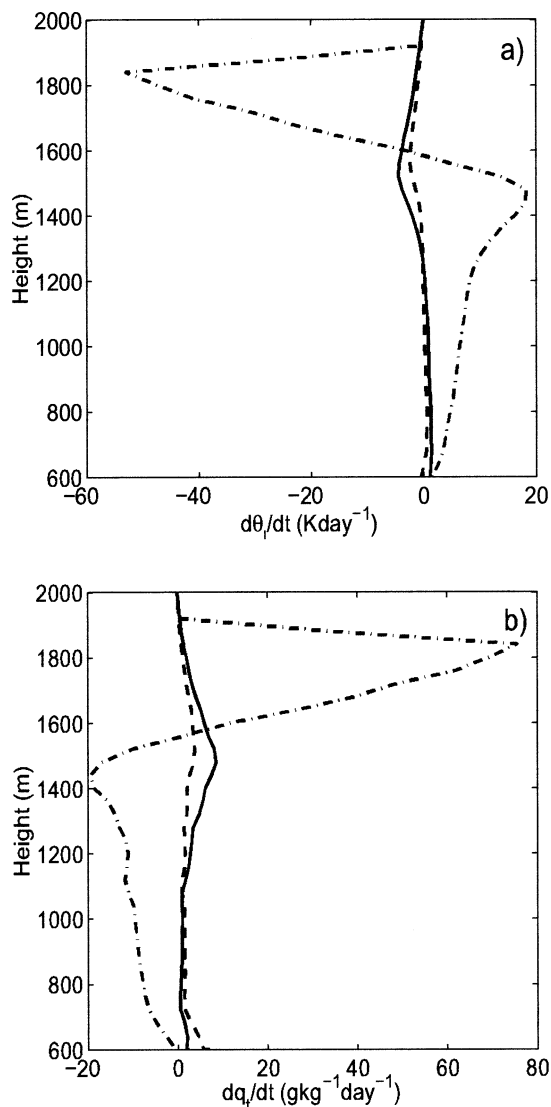


FIG. 15. (a) Net  $\theta$  tendencies and (b)  $q_1$  tendencies given three different detrainment criteria and the retrieved UER profile from Fig. 8b. Solid line is multimixing; dashed line is detrainment of all mixtures (single mixing) at their UNBL (following E91); dotted-dashed line is detrainment of all mixtures (single mixing) at their NBL (following RB86).

the environment at cloud top and warm and dry the environment at cloud base. The smallest clouds, in contrast, cool and moisten throughout their depth, as discussed in section 3d. Given the cumulative effect of the clouds, as represented by the large-scale forcing data (Figs. 6c,d), a size-distributed population is required, so that the cloud-top moistening effect of more numerous smaller clouds can counteract the cloud-base drying effect of less frequent larger clouds, with their larger undilute vertical mass flux and correspondingly larger convective transport-induced tendencies.

This counterbalancing transport requires a size distribution for which the cloud number density increases

monotonically with decreasing cloud size. An endpoint is reached for the smallest clouds in the ensemble, which only cool and moisten throughout their depth. These small clouds are also called forced clouds; they are little more than tracers of subcloud thermals, and do not vent subcloud air into upper levels or contribute to the cloud-scale circulation (Stull 1985). Nevertheless, these forced clouds play the important role of moistening and cooling throughout the shallow cloud-base layer, balancing heating and drying due to larger, deeper and more active clouds. The accurate representation of these cloud-base processes is crucial to the prediction of cloud-base thermodynamic properties, the cloud-base mass flux, and therefore the cloud-layer-subcloud-layer interaction.

Large eddy simulations have demonstrated the ability to reproduce many of the characteristics of the BOMEX boundary layer. Direct comparison between LES and the EMBS results presented here would be particularly useful. This requires that the LES be sampled using a definition of the cloud boundary that corresponds to that used in the EMBS model, where convective cloud includes the subsaturated near-cloud environment with its unsaturated downdrafts. The introduction of tracers would help reduce the uncertainty in determining the cloud convective envelope; we are currently conducting tracer studies using a high-resolution LES to quantify cumulus mixing and its associated convective mass flux, particularly for the evaluation of EMBS models.

An additional sampling requirement is that the effect of individual clouds be tracked through both growth and dissipation stages in the LES. This is necessary because the EMBS model tries to capture the net effect of these two stages using downward transport of cloud-environment mixtures to their UNBL. The EMBS model provides an example of the unified representation of condensation and evaporation through induced convective drafts rather than through direct local mixing and detrainment of liquid water. However, condensation and evaporation do show important differences in nonprecipitating cumuli. In particular, condensation may not necessarily be involved with mixing while evaporation is almost certainly associated with mixing. In this sense, the EMBS model can be interpreted as a simple representation of the cloud life cycle, with the growth phase/condensation represented by the upward transport of USCA, and the dissipation/evaporation phase represented by mixing and detrainment. Different representations of this life cycle are possible; recently von Salzen and McFarlane (2002) have developed a parameterization that accounts explicitly for the dissipation phase through a final detrainment term.

The EMBS models' symmetric treatment of condensation and evaporation through convective drafts is physically appealing, given that the two processes both rapidly influence the temperature of the far field environment but are confined to small turbulent regions. In the EMBS model, these downdrafts produce net downward mass flux within the inversion layer; observations

indicate that they are a dominant feature of the dissipation stage of shallow cumulus clouds. As we have shown here, the EMBS model requires no more free parameters than a bulk entraining and detraining plume model, given the UNBL detraining criterion and the demonstrated lack of sensitivity to the choice of the mixing distribution. We have also suggested that constraining the UER requires consideration of the cloud size distribution. Sensitivity studies are needed to determine how important the detailed specification of the UER is to the prognostic behavior of an EMBS parameterization of shallow convection.

*Acknowledgments.* We are grateful to Kerry Emanuel for providing his EMBS model and Pier Siebesma for providing results of the GCSS Boundary Layer Cloud Working Group BOMEX equilibrium soundings and forcings. The manuscript was significantly improved by the comments of Steven Esbensen and two anonymous reviewers. This work was supported through funding of the Modeling of Clouds and Climate Proposal by the Canadian Foundation for Climate and Atmospheric Sciences, the Meteorological Service of Canada, and the Natural Sciences and Engineering Research Council.

## APPENDIX A

### Notation

$E^i$	Undilute eroding rate at level $i$
$U^i$	Eroded USCA mass flux at level $i$
$F^b$	Undilute cloud-base mass flux
$F^{i+1/2}$	Upward flux of USCA at an interface level $i + 1/2$
$MF^{n,i}$	Total mixture-induced mass flux at level $n$ due to the eroding of USCA at level $i$ , normalized by $U^i$
$DT^{n,i}$	Total mixture-induced detraining of $\theta_i$ at level $n$ due to the eroding of USCA at level $i$ , normalized by $U^i$
$DQ^{n,i}$	Total mixture-induced detraining of $q_i$ at level $n$ due to the eroding of USCA at level $i$ , normalized by $U^i$
$\sigma^j$	Fraction of environment air in the $j$ th mixture
$P(\sigma^j)$	Normalized distribution of the eroded USCA in the generated spectrum of mixtures
$u^{i,j}$	Eroded USCA mass flux component in mixture $j$ generated at level $i$
$m^{i,j}$	Total mass flux of mixture $j$ generated at level $i$
$\theta_{i_v}^{i,j}$	Virtual potential temperature (including liquid water loading) of mixture $j$ generated at level $i$
$\theta_l^{i,j}$	Liquid water potential temperature of mixture $j$ generated at level $i$
$\theta_{i_v}^{i,j}$	Liquid water virtual potential temperature of mixture $j$ generated at level $i$
$q_t^{i,j}$	Total water specific humidity of mixture $j$ generated at level $i$

$\theta_v^i$	Environmental virtual potential temperature at level $i$
$\theta_l^i$	Environmental liquid water potential temperature at level $i$
$q_t^i$	Environmental total water specific humidity at level $i$
$\theta_l^u$	Liquid water potential temperature of USCA
$q_t^u$	Total water specific humidity of USCA
$\rho$	Air density
$g$	Acceleration due to gravity
$\mathbf{V}_H$	Large-scale horizontal wind
$w$	Large-scale subsidence (in $\text{m s}^{-1}$ )
$Q_R$	Radiation-induced temperature tendency
$M_f$	Averaged vertical cloud mass flux (in $\text{kg m}^{-2} \text{s}^{-1}$ )
$D$	Detrainment rate of cloud air mass (in $\text{kg m}^{-2} \text{s}^{-1} \text{Pa}^{-1}$ )

## APPENDIX B

### Multimixing of Positively Buoyant Mixtures

To account for further mixing of positively buoyant mixtures we group them and calculate their total mass flux:

$$S = \sum_{\{j'\}}^{\theta_{i_v}^{i,j'} > \theta_i^i} m^{i,j'} = \sum_{\{j'\}}^{\theta_{i_v}^{i,j'} > \theta_i^i} \frac{P(\sigma^j)}{1 - \sigma^j} U^i = B^i U^i, \quad (\text{B1})$$

and the averaged  $\theta_i$  and  $q_i$ :

$$\theta_i^s = \frac{\sum_{\{j'\}} m^{i,j} \theta_{i_v}^{i,j}}{\sum_{\{j'\}} m^{i,j}} = \frac{\sum_{\{j'\}} \frac{P(\sigma^j)}{1 - \sigma^j} \theta_{i_v}^{i,j}}{\sum_{\{j'\}} \frac{P(\sigma^j)}{1 - \sigma^j}}, \quad (\text{B2a})$$

$$q_i^s = \frac{\sum_{\{j'\}} m^{i,j} q_t^{i,j}}{\sum_{\{j'\}} m^{i,j}} = \frac{\sum_{\{j'\}} \frac{P(\sigma^j)}{1 - \sigma^j} q_t^{i,j}}{\sum_{\{j'\}} \frac{P(\sigma^j)}{1 - \sigma^j}}. \quad (\text{B2b})$$

Note that  $U^i$  cancels from the expressions for  $\theta_i^s$  and  $q_i^s$ . This makes the mass flux and the detraining contributions due to further mixing depend linearly on the initially eroded  $U^i$ .

We let the homogenized parcel  $S$  ascend to the next higher level  $i + 1$  (the ascending  $S$ -induced upward mass flux is added to  $MF^{n,i}$ ), pursue further mixing with the environment at level  $i + 1$ , and generate a new spectrum of mixtures:

$$\hat{m}^{i,j} = \frac{P(\sigma^j)}{1 - \sigma^j} S = \frac{P(\sigma^j)}{1 - \sigma^j} B^i U^i = C^{i,j} U^i. \quad (\text{B3})$$

The spectrum of newly generated mixtures  $\hat{m}^{i,j}$  is treated in the same way as in the initial mixing; that is, neutrally and negatively buoyant mixtures are detrained and positively buoyant mixtures are grouped and continue their ascent and further mixing. The mixtures'

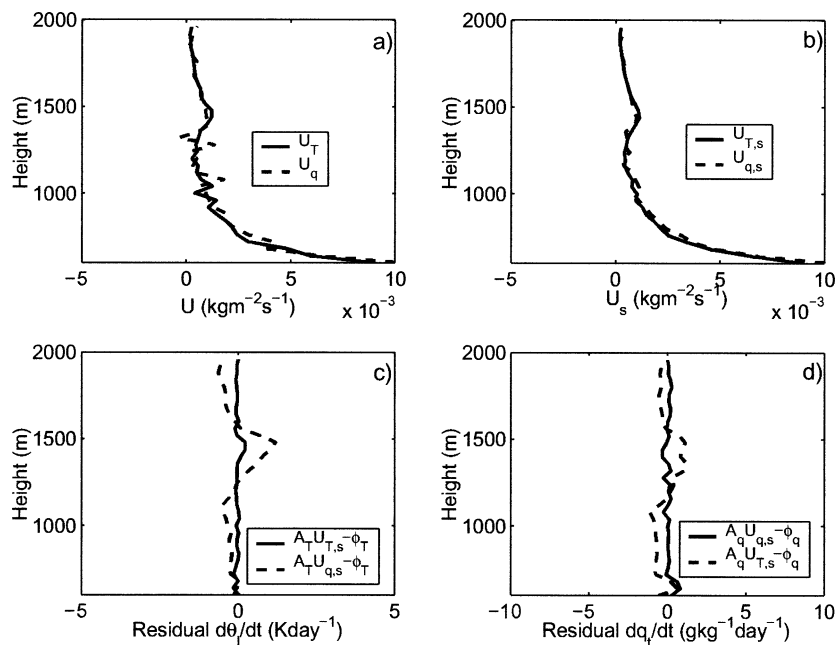


FIG. C1. (a) Exact solutions of (C1a) ( $U_T$ , solid line) and (C1b) ( $U_q$ , dashed line) calculated by direct inversion. (b) Smoothed solutions ( $U_{T,s}$ ,  $U_{q,s}$ ) of (a) after applying a three-point running average. (c) Residual tendencies from (C1a) given the smoothed solutions  $U_{T,s}$  and  $U_{q,s}$ , that is,  $A_T U_{T,s} - \phi_T$  (solid line) and  $A_T U_{q,s} - \phi_T$  (dashed line). (d) Residual tendencies from (C1b) given the smoothed solutions, that is,  $A_q U_{q,s} - \phi_q$  (solid line) and  $A_q U_{T,s} - \phi_q$  (dashed line).

buoyancy is evaluated at the current mixing level and their contribution to the mass flux is calculated based on the current mixing level and their detrainment level. The detrained mixtures' induced mass flux and detrainment tendencies are added to  $MF^{n,i}$ ,  $DT^{n,i}$ , and  $DQ^{n,i}$  through (7). The multimixing events [(B1)–(B3)] continue until further mixing between the grouped positively buoyant mixtures and their environment generate only neutrally and negatively buoyant mixtures or cloud top is reached. In practice, the multimixing process always stops well before cloud top due to the continuous homogenization and dilution of the positively buoyant mixtures. The multimixing process completes the  $U^i$  mixing initiated at level  $i$ .

## APPENDIX C

### Consistency and Stability of the UER Inversion

#### a. Consistency of solutions

We rewrite (8) in matrix form:

$$\mathbf{A}_T \mathbf{U} = \boldsymbol{\phi}_T, \quad (\text{C1a})$$

$$\mathbf{A}_q \mathbf{U} = \boldsymbol{\phi}_q, \quad (\text{C1b})$$

where  $\mathbf{U}$ ,  $\boldsymbol{\phi}_T$ , and  $\boldsymbol{\phi}_q$  are, respectively, vectors of eroded USCA mass flux and the total large-scale forcings of  $\theta_i$  and  $q_i$ ;  $\mathbf{A}_T$  and  $\mathbf{A}_q$  are  $\theta_i$  and  $q_i$  coefficient matrices generated using (8) with a specified mixing distribution

and the UNBL detrainment criterion with the multimixing treatment of positively buoyant mixtures;  $\mathbf{A}_T$  and  $\mathbf{A}_q$  have dimensions of  $M \times M$ , where  $M = 35$  is the number of vertical cloud levels; and the model's vertical resolution is 40 m.

Since (C1a) and (C1b) provide two constraints on one quantity  $U$  we may solve (C1a) and (C1b) independently. However, due to uncertainties in the specified soundings and large-scale forcings of  $\theta_i$  and  $q_i$ , we do not expect a single  $U$  to satisfy both equations exactly. Below, we compare these two  $\mathbf{U}$  solutions as a check on the consistency of the retrieval, using mixing distribution P1 (solutions using other mass distributions yield similar results). Since both  $\mathbf{A}_T$  and  $\mathbf{A}_q$  are well conditioned, we may invert both (C1a) and (C1b) directly.<sup>C1</sup>

Figure C1a shows a comparison between  $U$  retrieved by the direct inversion (i.e., multiplication by  $\mathbf{A}_{T/q}^{-1}$ ) of (C1a) and (C1b). The comparison shows good agreement between the two retrievals, although both profiles exhibit small-scale variability, a feature also seen below when we introduce noise into  $\mathbf{A}_T$  or  $\boldsymbol{\phi}_T$ . Figure C1b shows the solutions of Fig. C1a after applying a three-

<sup>C1</sup> Condition numbers are  $\mathbf{A}_{T1} = 153.21$ ,  $\mathbf{A}_{T2} = 153.03$ ,  $\mathbf{A}_{T3} = 8567.73$ ,  $\mathbf{A}_{T4} = 145.72$ ,  $\mathbf{A}_{q1} = 83.47$ ,  $\mathbf{A}_{q2} = 164.00$ ,  $\mathbf{A}_{q3} = 750.06$ , and  $\mathbf{A}_{q4} = 162.60$ , given multimixing and the UNBL detrainment criterion, with  $\mathbf{A}_{Tn/qn}$  denoting the condition number for mixing distribution  $P_n$ .

point running average. When the smoothed solutions  $\mathbf{U}_{T,s}$  and  $\mathbf{U}_{q,s}$  are inserted into the corresponding equations (C1a) and (C1b) the residual tendencies are very small (see solid lines in Figs. C1c,d), with  $\|\mathbf{A}_T \mathbf{U}_{T,s} - \phi_T\|/\|\phi_T\| = 0.04$  and  $\|\mathbf{A}_q \mathbf{U}_{q,s} - \phi_q\|/\|\phi_q\| = 0.06$  (where  $\|\cdot\|$  is the vector norm). When we cross-substitute the smoothed solution  $\mathbf{U}_{T,s}$  into (C1b), and  $\mathbf{U}_{q,s}$  into (C1a), the residual tendencies are  $\|\mathbf{A}_q \mathbf{U}_{T,s} - \phi_q\|/\|\phi_q\| = 0.18$  and  $\|\mathbf{A}_T \mathbf{U}_{q,s} - \phi_T\|/\|\phi_T\| = 0.23$  (see dashed lines in Figs. C1c,d).

We find similar residuals when we try to reproduce the  $\theta_i$  or  $q_i$  budgets using a bulk entraining and detraining plume model with diagnosed parameters from one of the budget equations. This suggests that the slightly larger residual tendencies found with cross-substitution are due to the imperfect coupling of  $\theta_i$  and  $q_i$  in the large-scale forcing and environmental sounding data; that is, when any cloud model exactly reproduces the budget equation (1a) it will produce a residual tendency in (1b) (and vice versa). Nevertheless, such differences are within the uncertainties of the LES residual tendencies. (P. Siebesma 2002, personal communication; available online at <http://www.knmi.nl/siebesma/gcss/tend3d.html>.)

In addition to direct inversion we have also used linear least-squares to solve (C1) subject to a smoothness constraint. This approach yields solutions nearly identical to the direct retrievals of Fig. C1b.

### b. Stability of solutions

As mentioned above, the  $\mathbf{A}_{T,q}$  coefficient matrices for all mixing distributions are characterized by small condition numbers. We therefore expect  $\mathbf{U}$  solutions to be insensitive to the introduction of noise through round-off errors. In the following, we further explore the sensitivity of the retrieved  $\mathbf{U}$  to noise that may exist in the soundings or large-scale forcings. In this calculation each term  $\phi_T^n$  of the forcing vector  $\phi_T$  is replaced by a perturbation of the form

$$\phi_T^n = \phi_T^n (1 + \alpha \eta), \quad (\text{C2})$$

where  $\eta$  is a uniformly distributed random number in the range  $(-1, 1)$  and  $\alpha$  is an amplitude in the range  $[0, 0.15]$ .

Figure C2a shows  $\mathbf{U}$  solutions obtained for different noise levels applied to the forcing for  $\theta_i$  Eq. (C1a). In Fig C2b, the noisy  $\mathbf{U}$  solutions are smoothed with a three-point running mean as in section 3. As Figs. C2a,b show, although the exact solutions vary with the introduction of noise, the three smoothed solutions are nearly identical. In Fig. C2c we insert the smoothed solutions into (C1a) and plot the residual tendency  $\mathbf{A}_T \mathbf{U}_{T,s} - \phi_T$ ; the residual tendencies are very small at all levels. The largest of the normalized deviations (defined by  $\|\mathbf{A}_T \mathbf{U}_{T,s} - \phi_T\|/\|\phi_T\|$ ), is 0.07. Repeating the random perturbation procedure for the coefficient matrix  $\mathbf{A}_T$ , other

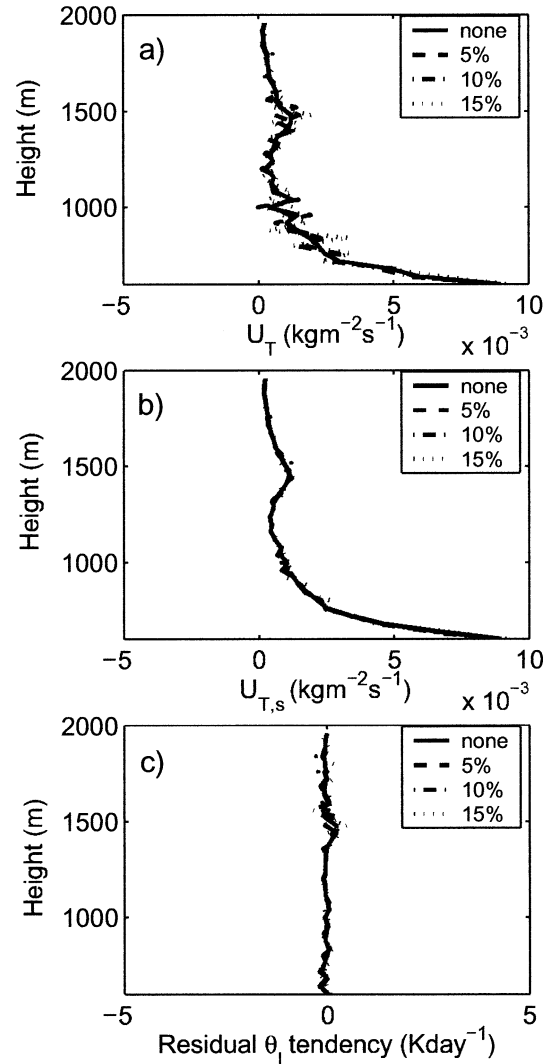


FIG. C2. Sensitivity of the solution of (C1a) to noise in the forcing term  $\phi_T$  with relative perturbation magnitudes in the range  $[0, 0.15]$  (see text). (a) Exact solutions given by direct inversion of (C1a). (b) As in (a), but smoothed by a three-point running mean. (c) The residual tendencies produced by substituting the smoothed solutions into (C1a).

mixing distributions P2–P4, and the  $q_i$  equation (C1b) yields similar results.

### REFERENCES

- Arakawa, A., and W. H. Schubert, 1974: Interaction of a cumulus cloud ensemble with the large-scale environment. Part I. *J. Atmos. Sci.*, **31**, 674–701.
- Austin, P. H., M. B. Baker, A. M. Blyth, and J. B. Jensen, 1985: Small-scale variability in warm continental cumulus clouds. *J. Atmos. Sci.*, **42**, 1123–1138.
- Benner, T. C., and J. A. Curry, 1998: Characteristics of small tropical cumulus clouds and their impact on the environment. *J. Geophys. Res.*, **103**, 28 753–28 767.
- Betts, A. K., 1973: A relationship between stratification, cloud depth, and permitted cloud radii. *J. Appl. Meteor.*, **12**, 890–893.

- Blyth, A. M., 1993: Entrainment in cumulus clouds. *J. Appl. Meteor.*, **32**, 626–641.
- , W. A. Cooper, and J. B. Jensen, 1988: A study of the source of entrained air in Montana cumuli. *J. Atmos. Sci.*, **45**, 3944–3964.
- Bretherton, C. S., and P. K. Smolarkiewicz, 1989: Gravity waves, compensating subsidence and detrainment around cumulus clouds. *J. Atmos. Sci.*, **46**, 740–759.
- Cahalan, R. F., and J. H. Joseph, 1989: Fractal statistics of cloud fields. *Mon. Wea. Rev.*, **117**, 261–272.
- Carpenter, R. L., J. K. K. Droegemeier, and A. M. Blyth, 1998: Entrainment and detrainment in numerically simulated cumulus congestus clouds. Part III. Parcel analysis. *J. Atmos. Sci.*, **55**, 3440–3455.
- Cohen, C., 2000: A quantitative investigation of entrainment and detrainment in numerically simulated cumulonimbus clouds. *J. Atmos. Sci.*, **57**, 1657–1674.
- de Roode, S. R., and C. S. Bretherton, 2003: Mass-flux budgets of shallow cumulus clouds. *J. Atmos. Sci.*, **60**, 137–151.
- Duynkerke, P., 1998: Dynamics of cloudy boundary layers. *Clear and Cloudy Boundary Layers*, A. Holtslag and P. Duynkerke, Eds., Royal Netherlands Academy of Arts and Sciences, 199–218.
- Emanuel, K. A., 1991: A scheme for representing cumulus convection in large-scale models. *J. Atmos. Sci.*, **48**, 2313–2335.
- , 1994: *Atmospheric Convection*. Oxford University Press, 580 pp.
- , and M. Zivkovic-Rothman, 1999: Development and evaluation of a convection scheme for use in climate models. *J. Atmos. Sci.*, **56**, 1766–1782.
- Esbensen, S., 1978: Bulk thermodynamic effects and properties of small tropical cumuli. *J. Atmos. Sci.*, **35**, 826–837.
- Heymsfield, A. J., P. N. Johnson, and J. E. Dye, 1978: Observations of moist adiabatic ascent in northeast Colorado cumulus congestus clouds. *J. Atmos. Sci.*, **35**, 1689–1703.
- Hu, Q., 1997: A cumulus parameterization based on a cloud model of intermittently rising thermals. *J. Atmos. Sci.*, **54**, 2292–2307.
- Jensen, J. B., P. H. Austin, M. B. Baker, and A. M. Blyth, 1985: Turbulent mixing, spectral evolution and dynamics in a warm cumulus cloud. *J. Atmos. Sci.*, **42**, 173–192.
- Kain, J. S., and J. M. Fritsch, 1990: A one-dimensional entraining/detraining plume model and its application in convective parameterization. *J. Atmos. Sci.*, **47**, 2784–2802.
- Kollias, P., B. A. Albrecht, R. Lhermitte, and A. Savtchenko, 2001: Radar observations of updrafts, downdrafts and turbulence in fair-weather cumuli. *J. Atmos. Sci.*, **58**, 1750–1766.
- Kuo, K., R. M. Welch, and R. C. Weger, 1993: The three-dimensional structure of cumulus clouds over the ocean: Structural analysis. *J. Geophys. Res.*, **98**, 20 685–20 711.
- Neggers, R. A., A. Siebesma, and H. Jonker, 2002: A multiparcel model for shallow cumulus convection. *J. Atmos. Sci.*, **59**, 1655–1668.
- , H. J. Jonker, and A. P. Siebesma, 2003: Size statistics of cumulus cloud populations in large-eddy simulations. *J. Atmos. Sci.*, in press.
- Nitta, T., 1975: Observational determination of cloud mass flux distributions. *J. Atmos. Sci.*, **32**, 73–91.
- , and S. Esbensen, 1974: Heat and moisture budget analyses using BOMEX data. *Mon. Wea. Rev.*, **102**, 17–28.
- Paluch, I. R., 1979: The entrainment mechanism in Colorado cumuli. *J. Atmos. Sci.*, **36**, 2467–2478.
- Plank, V. G., 1969: The size distribution of cumulus clouds in representative Florida populations. *J. Appl. Meteor.*, **8**, 46–67.
- Raymond, D. J., and A. M. Blyth, 1986: A stochastic mixing model for nonprecipitating cumulus clouds. *J. Atmos. Sci.*, **43**, 2708–2718.
- Siebesma, A. P., 1998: Shallow cumulus convection. *Buoyant Convection in Geophysical Flows*, E. J. Plate et al., Eds., Kluwer Academic, 441–486.
- , and J. Cuijpers, 1995: Evaluation of parametric assumptions for shallow cumulus convection. *J. Atmos. Sci.*, **52**, 650–666.
- , and A. Holtslag, 1996: Model impacts of entrainment and detrainment rates in shallow cumulus convection. *J. Atmos. Sci.*, **53**, 2354–2364.
- , and Coauthors, 2003: A large eddy simulation intercomparison study of shallow cumulus convection. *J. Atmos. Sci.*, in press.
- Simpson, J., 1971: On cumulus entrainment and one-dimensional models. *J. Atmos. Sci.*, **28**, 449–455.
- Stull, R. B., 1985: A fair-weather cumulus cloud classification scheme for mixed-layer studies. *J. Appl. Meteor.*, **24**, 49–56.
- Taylor, G. R., and M. B. Baker, 1991: Entrainment and detrainment in cumulus clouds. *J. Atmos. Sci.*, **48**, 112–121.
- Telford, J. W., 1975: Turbulence, entrainment, and mixing in cloud dynamics. *Pure Appl. Geophys.*, **113**, 1067–1084.
- von Salzen, K., and N. A. McFarlane, 2002: Parameterization of the bulk effects of lateral and cloud-top entrainment in transient shallow cumulus clouds. *J. Atmos. Sci.*, **59**, 1405–1430.
- Warner, J., 1970: On steady-state one-dimensional models of cumulus convection. *J. Atmos. Sci.*, **27**, 1035–1040.